Journal for ImmunoTherapy of Cancer

Hyaluronic acid-CD44 signaling defines therapeutic resistance and immunosuppressive microenvironment in peritoneal metastasis of gastric cancer

Junjie Zhao,[1,2] Chengbo Ji ,[1,2] Jie Sun,[1,2] Chenyu Tian,[1,2] Tianyi Cai,[1,2] Zhaoming Wang,[1,2] Zhaodong Sun,[1,2] Bosen Li,[3] Guoxing Ma,[1,2] Dan Liu ,[1,2] Masami Yamamoto,[4] Tetsuya Tsukamoto,[5] Sachiyo Nomura,[6] Liming Sun,[7] Yihong Sun,[1,2,3] Liyu Huang,[8,9] Yuanyuan Ruan,[1,10] Haojie Li,[1,2,3] Xuefei Wang [1,2,3,11]

To cite: Zhao J, Ji C, Sun J, *et al*. Hyaluronic acid-CD44 signaling defines therapeutic resistance and immunosuppressive microenvironment in peritoneal metastasis of gastric cancer. *Journal for ImmunoTherapy of Cancer* 2026;**14**:e014179. doi:10.1136/jitc-2025-014179

► Additional supplemental material is published online only. To view, please visit the journal online (https://doi.org/10.1136/jitc-2025-014179).

JZ, CJ and JS contributed equally.

Accepted 09 February 2026

Check for updates

© Author(s) (or their employer(s)) 2026. Re-use permitted under CC BY-NC. No commercial re-use. See rights and permissions. Published by BMJ Group.

For numbered affiliations see end of article.

Correspondence to
Dr Haojie Li;
li.haojie@zs-hospital.sh.cn

Dr Liyu Huang;
huangly@sjtu.edu.cn

Professor Yuanyuan Ruan;
ryyfdu@126.com

Dr Xuefei Wang;
wang.xuefei@zs-hospital.sh.cn

ABSTRACT

Background Peritoneal metastasis (PM) is one of the most challenging clinical problems in gastric cancer (GC), largely due to its high recurrence rate and poor response to current therapies. Increasing evidence indicates that remodeling of the extracellular matrix (ECM) plays an important role in therapeutic failure. However, how specific stromal–immune interactions contribute to PM heterogeneity and immunotherapy resistance remains unclear. In this study, we investigated how ECM composition—particularly the accumulation of hyaluronic acid (HA)—influences the immune microenvironment and therapeutic responses in GC-associated PM.

Methods We combined histopathological assessment, analyses of patient-derived specimens, single-cell transcriptomic profiling, and murine models of PM to delineate ECM remodeling patterns and immune cell dynamics in therapy-sensitive and therapy-resistant lesions. In addition, functional assays and pharmacological approaches were used to examine HA–CD44 signaling and its impact on $CD4^+$ T cell differentiation and responsiveness to immune checkpoint blockade.

Results Therapy-sensitive PM lesions were characterized by enrichment of elastic fibers, whereas therapy-resistant lesions showed collagen accumulation. Notably, HA deposition emerged as a key feature distinguishing these ECM states and was closely associated with differential therapeutic outcomes. Elevated HA levels activated CD44-dependent signaling in $CD4^+$ T cells, driving regulatory T cell (Treg) differentiation through a CD44–IQGAP1–RAC1–SMAD3 signaling pathway and thereby establishing an immunosuppressive microenvironment. Importantly, pharmacological inhibition of CD44 reduced Treg expansion and markedly enhanced the antitumor efficacy of anti-PD-1 therapy in murine PM models.

Conclusions Our findings identify HA–CD44 signaling as a critical link between ECM remodeling and immune evasion in GC PM. Targeting ECM-driven immunosuppressive mechanisms may represent a promising strategy to overcome therapeutic resistance and improve the efficacy of immunotherapy in this aggressive disease.

WHAT IS ALREADY KNOWN ON THIS TOPIC

⇒ Peritoneal metastasis (PM) from gastric cancer (GC) is associated with extensive stromal remodeling, limited drug delivery and marked immune suppression, leading to very poor survival.

⇒ Hyaluronic acid (HA)–CD44 signaling is involved in cancer progression and immune modulation, but its role in shaping the peritoneal metastatic microenvironment and resistance to immunotherapy is not well established.

⇒ Although regulatory T cells (Tregs) are known to accumulate in peritoneal metastases and correlate with poor prognosis, the upstream stromal drivers of this enrichment remain unclear.

WHAT THIS STUDY ADDS

⇒ This study identifies impaired tumor-cell HA degradation as a key driver of HA accumulation, defining an immunosuppressive and treatment-resistant peritoneal niche.

⇒ $CD44^+CD4^+FOXP3^+$ Tregs represent the predominant CD44-expressing immune population in HA-rich peritoneal lesions, and their differentiation is promoted through a CD44–IQGAP1–RAC1–SMAD3 signaling pathway.

⇒ In both patient-derived samples and mouse models, CD44 blockade reduces Treg abundance, restores cytotoxic T cell activity, and enhances the therapeutic response to anti-PD-1 treatment.

INTRODUCTION

Gastric cancer (GC) is the fifth most common cancer worldwide and the third leading cause of global cancer mortality.[1] Peritoneal metastasis (PM) is the most common type of

HOW THIS STUDY MIGHT AFFECT RESEARCH, PRACTICE OR POLICY

⇒ These findings position the HA–CD44 axis as a clinically relevant stromal–immune checkpoint in GC PM.
⇒ They support the evaluation of CD44-targeted therapies in combination with PD-1 inhibitors and suggest HA/CD44 features, including CD44$^+$ Tregs, as potential biomarkers for patient selection.
⇒ Incorporating assessment of matrix composition and HA–CD44 status may improve stratification and treatment planning for patients with peritoneal dissemination.

metastasis in GC,[2 3] and the prognosis of patients with PM is approximately 3–9 months on account of ineffective treatments.[4 5] Several systemic therapies have been introduced in the past two decades for the treatment of metastatic GC with limited progression as the presence of the plasma-peritoneal barrier and the poor blood supply of PM limit the tissue penetration and therapeutic effect of systemic agents.[6] This highlights the urgent need to elucidate the molecular mechanisms underlying peritoneal dissemination and identify novel therapeutic targets.

A key feature of the peritoneal metastatic niche is its unique extracellular matrix (ECM), where hyaluronic acid (HA) has emerged as a critical regulator.[6] Elevated HA synthesis increases the density and stiffness of the matrix, thereby enhancing interstitial pressure and facilitating tumor cell attachment, migration, and survival on the mesothelial surface.[7–11] Mechanistically, HA interacts with specific receptors such as CD44, LYVE1, and ICAM1, activating multiple downstream signaling pathways that promote epithelial-mesenchymal transition and angiogenesis.[9 11 12] Beyond its structural roles, an HA-enriched matrix also acts as a physical and biochemical barrier limiting drug diffusion and altering immune cell activity.[9 13] However, the specific role of HA in gastric tumor peritoneal dissemination and its underlying mechanism remain poorly defined.

Cancer metastasis is a complex, multistep process involving interactions between tumor cells and the tumor microenvironment.[14] Tumor cells derived from the gastrointestinal tract reach the peritoneum and attempt to implant into the peritoneum to form metastases, which requires their 'close cooperation' with normal peritoneal cells.[15] In addition, tumor cells must evade local immune responses for successful colonization.[16] Although CD8$^+$ T cells and natural killer (NK) cells suppress the primary or metastatic tumor cells,[17 18] tumor cells and metastatic derivatives have developed ways to overcome these immune responses, partly by recruiting immunosuppressive cells.[19] Among these immune cells, regulatory T cells (Treg) have emerged as critical mediators of immunosuppression in various cancers, including GC.[20] Emerging evidence suggests that Tregs are particularly abundant in peritoneal metastases of GC and correlate with poor clinical outcomes.[20 21]

In this study, we found that excessive HA deposition in PM lesions contributes to immune evasion and treatment resistance via the HA-CD44 axis. As a principal cell surface receptor for HA, CD44 mediates cell-cell and cell-matrix interactions and regulates multiple signaling pathways involved in cell proliferation, migration, and survival.[22 23] We revealed that the HA-CD44 axis promotes PM of GC through modulation of Treg differentiation. Mechanistically, we identified a novel interaction between CD44, IQGAP1, and RAC1 that activates Smad3 signaling, thus promoting FOXP3 expression. Targeting CD44 enhances the efficacy of Programmed cell death protein-1 (PD-1) blockade in preclinical models of GC PM, providing a rationale for combination immunotherapy approaches. Our findings reveal a previously unrecognized mechanism of immunosuppression in GC and identify the HA-CD44 axis as a potential therapeutic target for improving outcomes in patients with PM.

MATERIALS AND METHODS

Sample collection and tissue processing

A total of 14 patients with GC diagnosed with PM in Zhongshan Hospital were enrolled in this study. For ascites and peritoneal lavage fluid, a large amount of ascites (>200 mL) was aspirated, while patients with less ascites (<200 mL) were treated with abdominal cavity lavage with 500 mL warm saline, and the same procedure was performed afterwards. Samples for flow cytometry and fluorescence-activated cell sorting (FACS) were collected during laparoscopic exploration with laparoscopic scissors or ultrasonic scalpels followed by complete hemostasis. The detailed clinical and histopathological characteristics of this cohort are described in online supplemental table S1. Tissues collected from the peritoneum and omentum were trimmed carefully to snip away as much adipose tissue as possible, cut into small pieces (2×2 mm^2) and washed with phosphate-buffered saline (PBS) containing 2% fetal bovine serum (FBS). Tissues were then digested in 4 mL Roswell Park Memorial Institute (RPMI)−1640 medium (Gibco, USA) supplemented with 2% FBS (Biological Industries, Israel), 10 mg/mL collagenase type II (Worthington, USA), and 1 mg/mL deoxyribonuclease I (Worthington, USA) and incubated at 37 °C for 2 hours while gently shaking, and further processed with a gentleMACS Dissociator (Miltenyi Biotech, Germany). After digestion, tissues were washed twice and filtered through a 70 µm cell strainer (Corning, USA) to obtain single-cell suspensions.

Patient-derived peritoneal carcinomatosis cells

Ascites samples ranging from 200 mL to 3,000 mL were obtained from the patients with gastric adenocarcinoma (GAC) mentioned above and handled following the protocol in another study.[24] All ascites cells were spun down at 2000×g for 20 min, and then pelleted cells were lysed in red blood cell lysis buffer (Beyotime Biotechnology, China). Cytological confirmation and the percentage of malignant cells based on each sample were recorded by a pathologist or cytologist.

Flow cytometry and FACS

A single-cell suspension of each sample was freshly prepared, following the above dissociation step and red blood cell depletion. Then, the cell suspensions were stained with the selected antibodies (online supplemental table S2), and each sample was stained with antibodies at 4°C for 30 min. After washing, the cells were set and sorted twice using a BD LSRFortessa instrument (BD Bioscience, USA). Dead cells, debris, and doublet depletion were applied prior to analysis and acquisition. All sorted live cells were cultured in RPMI-1640 (Gibco, USA) with 10% FBS (Biological Industries, USA).

Flow cytometry data analysis

Flow cytometry FCS (Flow Cytometry Standard) files were uploaded and evaluated using Cytobank software (https://premium.cytobank.cn/cytobank, Beckman Coulter Life Sciences, USA).[25] Visual stochastic neighbor embedding (viSNE) was manipulated for dimensionality reduction. viSNE plots were generated with the following parameters: desired total events (equal sampling): 10 000 per group; channels: all six fluorescence antibody channels; compensation: file-internal compensation; iterations: 1000; perplexity: 30; and theta: 0.5.

Immunohistochemistry

Optimization of immunohistochemistry (IHC) staining was based on the protocol we used in our previous studies.[26] Tissues were fixed with 10% neutral buffered formalin, dehydrated, and embedded in paraffin. Sections (4 µm thick) were cut from formalin-fixed, paraffin-embedded tissue blocks. After deparaffinization, slides were subjected to an antigen retrieval procedure in 10 mM sodium citrate buffer (pH=6.0) for 3 min using a microwave. Slides were incubated in methanol containing 0.3% hydrogen peroxide for 20 min at room temperature to block endogenous peroxidase activity before applying the blocking solution. A 5% bovine serum albumin (BSA) solution was used as a blocking buffer. Then, slides were incubated with primary antibodies at 4°C overnight. IHC was performed with primary antibodies listed in online supplemental table S3. Slides were then incubated with a biotin-conjugated secondary antibody for 30 min, followed by peroxidase-conjugated streptavidin incubation for 30 min at room temperature. Peroxidase activity was detected using the substrate DAB (3,3′-Diaminobenzidine). For histologic evaluation, sections were stained with H&E. The percentage of different antibody-positive cells is shown as IHC scores (intensity × number, Intensity: 0, none; 1, mild; 2, moderate; 3, strong; 4, severe. Number: 1, 0%–25%; 2, 25%–50%; 3, 50%–75%; 4, 75%–100%).

Multiplex IHC

For multiplex IHC (mIHC) staining, IHC antibodies were used as indicated in online supplemental table S3. A multiple fluorescent immunohistochemical staining kit (pika universal secondary antibody; Absin Bioscience, China) was used, and experiments were conducted following the manufacturer's instructions. First, the concentration and the application order of the three antibodies were optimized, and the spectral library was built based on the single-stained slides. The slides were first deparaffinized by xylene and ethanol, and antigen retrieval was performed by microwaving. After incubation with 3% H_2O_2 for 10 min, the tissues were blocked in blocking buffer for another 10 min at room temperature. Then, the tissues were incubated with primary antibody, secondary HRP, and TSA working solution. The slides were then mounted with antifade mounting medium with DAPI (Absin Bioscience, China). Analysis was performed with the HALO image analysis platform (Indica Labs, USA).

In vivo mouse model

For the peritoneal metastatic model employing human peripheral blood mononuclear cell (PBMC)-reconstituted NSG (NOD/Scid IL2Rγ^{null}) mice, murine GC cells or patient-derived peritoneal cancer cells were injected into the abdominal cavities according to a previous study.[27] 3×10^6 ascites cells were injected into the abdominal cavities of humanized NSG mice (n=6 per group). After 40–50 days, all the mice were sacrificed, and the number of peritoneal metastatic nodules was counted. Fresh subcutaneous tumor and metastatic nodule tissues were collected and fixed with formalin. The murine GC cell line YTN16 (C57BL/6-derived) was cultured in high-glucose Dulbecco's Modified Eagle Medium (DMEM, Gibco, USA) supplemented with 10% FBS according to the previous study.[28 29] For the peritoneal metastatic model, 1×10^7 of YTN16 cell lines in 200 uL PBS were injected into the abdominal cavities of C57BL/6 mice (C57; n=3–5 per group). Luciferase-labeled vector plasmid was constructed and packaged into lentivirus, followed by infecting the YTN16 cell line. The details of drug administration are listed in online supplemental table S4. After 40–50 days, all the mice were sacrificed, and the number and the weight of peritoneal metastatic nodules were calculated. Fresh metastatic nodule tissues were collected and fixed with formalin. For the in vivo experiments, animals were randomly assigned to treatment and control groups using a random number table. Investigators responsible for data collection and outcome assessment were blinded to the group allocation throughout the experiment.

Magnetic cell separation

$CD4^+$ T cell isolation from human PBMCs, ascites, and tumor-infiltrating lymphocytes was performed using the EasySep Human CD4+ T Cell Isolation Kit (STEMCELL Technologies, Canada, Catalog #17952) following the manufacturer's protocol. Treg isolation was performed by EasySep Human CD4+CD127lowCD25+Regulatory T Cell Isolation Kit (STEMCELL Technologies, Canada, Catalog #18063) following the manufacturer's protocol. $CD8^+$ T cells were isolated using EasySep Human CD8+

T Cell Isolation Kit (STEMCELL Technologies, Canada, Catalog #17953).

T cell culture and reagent usage

$CD4^+$ T cells were isolated as mentioned above. For Treg enrichment, $CD4^+CD25^+$ cells were further purified using the EasySep Human CD25 Positive Selection Kit II (STEMCELL Technologies, Canada, #17896). Cell viability (>95%) was confirmed by Trypan Blue exclusion, and purity (>92% $CD4^+CD25^+Foxp3^+$) was verified via flow cytometry. Cells were maintained in RPMI 1640 medium supplemented with: 10% heat-inactivated FBS (Gibco, USA, #26140087), 100 U/mL penicillin/streptomycin (Gibco, USA, #15140122), and 20 ng/mL recombinant human IL-2 (STEMCELL Technologies, Canada, #78036). Dynabeads Human T-Activator CD3/CD28 (Thermo Fisher, USA, #11 161D) at 1:1 bead-to-cell ratio was used for T cell activation. Cells were activated for 48 hours at 37°C/5% CO_2 before downstream assays. Naive $CD4^+$ T cells were polarized into induced Tregs (iTregs) using: 5 ng/mL recombinant human Transforming growth factor-beta 1 (TGF-β1, MedChemExpress, USA, HY-P7118) and 20 ng/mL recombinant human IL-2 (STEMCELL Technologies, Canada, #78036). Prior to Treg induction, T cells were treated with Angstom6, HA, anti-CD44, IQGAP1 inhibitor, RAC1 inhibitor, and TGFβR1 inhibitor repectively for 2 hours (details mentioned in online supplemental table S4). HA polymer (molecular weight 800–1500 kDa; MedChemExpress, USA, HY-B0633A) was used in in vitro studies based on literature evidence that high-molecular-weight HA preferentially engaged CD44 signaling. The HA preparation was confirmed to be endotoxin-free (Limulus Amebocyte Lysate (LAL) assay: <0.1 EU/mg). Specifically, HA was pretreated with bovine testicular hyaluronidase (Sigma, USA, 100 U/mL, 37°C for 2 hours) to degrade HA into small fragments.

Treg-$CD8^+$ T cell co-culture system

$CD8^+$ T cells were labeled with 5 µM CellTrace Violet (CTV, Thermo Fisher, USA, #C34571) and activated with Dynabeads Human T-Activator CD3/CD28 (Thermo Fisher, USA, #11 161D) at a 1:1 bead-to-cell ratio in RPMI-1640+10% FBS + 100 U/mL IL-2. Tregs were prestimulated with reagents mentioned in online supplemental table S4 and then stimulated with CD3/CD28 beads. Cells were co-cultured in 96-well U-bottom plates with a ratio of 1:1 (Corning, USA, #3799) at 37°C/5% CO_2 for 5 days both in the contact-dependent and soluble manner with 0.4 µm Transwell membrane. After that, FOXP3, Interferon-gamma (IFN-γ), and granzyme B (GZMB) were tested by flow cytometry.

Cell viability and apoptosis assays

Cell viability was assayed using the Cell Counting Kit-8 (Dojindo, Japan) according to the manufacturer's instructions. In the CCK8 assay, cells were inoculated into 96-well plates at 3000 cells per well. After incubation for the indicated time points, CCK-8 solution was added to each well and incubated for 60 min. The absorbance was measured at OD 450 nm using a BioTek Gen5 system (Biotech USA, USA). Cell apoptosis assay was performed by flow cytometry. Annexin V-APC/7-AAD apoptosis kit (Multi Sciences, China) was used, and cell staining was followed by the instruction protocol. Flow cytometry for apoptosis was conducted by BD LSRFortessa instrument (BD Bioscience, USA) and analyzed by FlowJo V.10 software.

Plasmid transfection

Plasmid transfection was performed with ProteanFect Max (Nanoportal Biotech, China) according to the manufacturer's recommendations. For CD44 overexpression, different fragments of CD44 and IQGAP1 were generated by subcloning the corresponding cDNAs into the pcDNA3.1-Flag-EGFP-vector and the pcDNA3-MYC-mcherry-vector, respectively.

Co-immunoprecipitation (Co-IP) and mass spectrometer analysis

Co-immunoprecipitation was performed by using the rProtein A/G Magnetic IP/Co-IP Kit (Absin, abs9649, China). Tregs were collected and lysed using IP lysis buffer following the manufacturer's protocol and the processed samples were analyzed by Liquid Chromatography-Tandem Mass Spectrometry (LC-MS/MS) on mass spectrometer or continued for immunoblotting. All data were stored at URL: https://www.iprox.cn/page/DSV021.html;?url=1761539159589HF0U.

Immunofluorescence staining

$CD44^+$ T cells were fixed for 1 hour at room temperature, washed, and processed for immunofluorescence staining. A 3% BSA solution was used as the blocking buffer. Then, the slides were incubated with primary antibodies against IQGAP1 (Proteintech, China, 1: 200 dilution) at 4°C overnight followed by incubation with goat antirabbit secondary antibody, Alexa Fluor 488 (Thermofisher, USA, 1:1000 dilution). The procedure was repeated from cell blocking followed by primary antibodies against CD44 (Cell Signaling Technology, USA, 1:200 dilution) and goat antimouse secondary antibodies TRITC-TSA (Tetramethylrhodamine isothiocyanate-Tyramide Signal Amplification) (Thermofisher, USA, 1:1000 dilution). Following this step, nuclei counterstaining was performed by incubating cells with DAPI (4′,6-diamidino-2-phenylindole) for 5 min at room temperature.

Immunoblotting

The cell lysates were extracted using RIPA lysis buffer with Protease and Phosphatase Inhibitor Cocktail (NCM Biotech, China). Cell lysates were electrophoresed on 10%–12% SDS-PAGE (Sodium Dodecyl Sulfate-Polyacrylamide Gel Electrophoresis) gels followed by transferring to Polyvinylidene fluoride (PVDF) membranes (Millipore, USA). The membranes were first blocked for non-specific binding in NCMBlot Blocking

Buffer (NCM Biotech, China) at room temperature for 10 min. Total protein lysates were immunoblotted with antibodies listed in online supplemental table S3 at 4°C overnight and incubated with a horseradish peroxidase-conjugated secondary antibody at room temperature for 1 hour. The bound antibody was detected with ECL (Enhanced Chemiluminescence) reagent (NCM Biotech, China). Protein expression was quantified by densitometry and normalized to GAPDH (Glyceraldehyde-3-phosphate dehydrogenase) expression levels with ImageJ software.

Quantitative real-time PCR

Total RNA was isolated from human GC cell lines using RNeasy Mini Kit (Qiagen, Germany) with DNase treatment (Qiagen, Germany). RNA was then transcribed using the PrimeScript RT Master Mix (Takara Bio, Japan). Quantitative real-time PCR was performed using QuantStudio 6 Flex System (ThermoFisher, USA). Gene expression was normalized to the expression of the housekeeping gene 18S. Relative fold changes were transformed using the comparative threshold cycle (CT) method (the $2^{-\Delta\Delta CT}$ method) with the QuantStudio Real-Time PCR Software. Primer sequences are provided below: 18S, F-CGGCTACCACATCCAAGGAA, R-GCTGGAATTACCGCGGCT; FOXP3, F-TGACCAAGGCTTCATCTGTG, R-GAGGAACTCTGGGAATGTGC.

ELISA

For ELISA, all the cytokines were tested in the cell supernatant from cell lines mentioned above by using the ELISA kit following the manufacturer's instructions (Multiscience Biotech, China).

Mesothelial clearance assay

The human-derived PC -04 (peritoneal carcinomatosis-04) cells, established above were filtered by the Tumor Cell Isolation Kit, human (Miltenyi Biotec, Germany) according to the manufacturer's protocol. The cells were then cultured in RPMI-1640 medium supplemented with 10% FBS and 1% L-glutamine (Gibco, USA). Human peritoneal mesothelial cell line HmrSV5 cells were cultured in DMEM supplemented with 10% FBS. PC-04 cells and HmrSV5 cells were transfected with Ubi-MCS-3FLAG-CBh-gcGFP-IRES-puromycin plasmid and Ubi-MCS-3FLAG-SV40-Cherry plasmid, respectively, through lentivirus infection. All the procedures were imitated according to the previous study.[30] The mesothelial cells were plated on glass-bottom dishes (Mat-TEK Corporation, USA) coated with 5 µg/mL of fibronectin (Sigma, USA) and/or collagen I (Sigma, USA). Cells were maintained in culture until confluent (48 hours after plating). PC-04 cells were washed two times with PBS, resuspended by trypsin-EDTA (Gibco, USA), and were added to a confluent mesothelial monolayer at 5×10^5 cells/mL, allowed to attach for 60 min, and imaged for the indicated time. Only cells that remained attached during the experiment were used for quantification.

Luciferase reporter assay

Cell extracts were prepared 48 hours after transfection, and luciferase activity was measured with the Dual Luciferase Reporter Gene Assay Kit (Yeasen Biotechnology, China) according to the manufacturer's protocols. All plasmids were purchased from Pullen Biotechnology, Shanghai, China.

Cohort of patients with GC with PM

Archival tissue samples were collected from 141 patients with GC with solely PM (M1) who were not treated before and underwent abdominal nodule biopsy or cytoreductive surgery from 2015 to 2021 in Zhongshan Hospital. 12 patients with GC with PM received immunotherapy after their PM tissues were collected through laparoscopic biopsy from 2019 to 2021 in Zhongshan Hospital.

Single-cell library preparation and sequencing

Cells were loaded onto the 10X Chromium Single Cell Platform (10X Genomics) at a concentration of 1000 cells per µL (Single Cell 5′ library and Gel Bead Kit V.2) as described in the manufacturer's protocol. Generation of gel beads in emulsion (GEMs), barcoding, GEM-RT (Gel Bead-in-Emulsion-reverse transcription) clean-up, complementary DNA amplification, and library construction were all performed as per the manufacturer's protocol. Qubit was used for library quantification before pooling. The final library pool was sequenced on the Illumina Novaseq 6000 instrument using 150-base-pair paired-end reads. Mapping to GRCh38 human genome, quality control and read counting of Ensembl genes was performed by cellranger software with default parameter (V.8.0.0).

Single-cell RNA sequencing data analysis

Single-cell RNA sequencing (scRNA-seq) data analyses were performed using R V.4.2.1. For quality control, cells were filtered using the following criteria: (1) Cells expressing fewer than 200 or greater than 2500 genes were excluded; (2) Cells with ≥10% of UMIs (Unique Molecular Identifiers) mapped to mitochondrial or ribosomal genes were removed. Doublets were detected using the DoubletFinder R package with recommended parameters. To detect the doublets, cells with UMI/gene numbers were eliminated from the limit of mean values±two fold of SD, and then the R package 'DoubletFinder'[31] was applied with the recommended parameters. Moreover, to remove the batch effects in scRNA-seq data, we performed analysis using the 'FindIntegrationAnchors'.[32] After quality normalization, the Seurat R package was used to analyze the scRNA-seq data using the 'FindVariableFeatures', 'FindClusters' (setting the 'resolution' parameter to 0.5), and 'FindAllMarkers' functions.[33] Finally, using the SingleR package[34] and CellMarker data set,[35] cell clusters were annotated with the dominant expression cell markers. We performed the trajectory analysis via the R package monocle3 to explore the tumor reprogramming processes in single cells. Gene expression density

was visualized using the 'Nebulosa' R package, which estimates kernel density-based gene expression distributions in low-dimensional embeddings.[36]

Statistical analyses

All data are shown as the mean±SD, and Student's *t*-test, Mann–Whitney *U* test, Wilcoxon signed-rank test, and χ^2 test were used in this study. Kaplan–Meier curves were constructed to determine the overall survival (OS) of patient and mouse subgroups and were evaluated by log-rank tests. Multivariate analyses of the Cox regression model were used to estimate HRs and 95% CIs. Covariate effects on survival and interactions between different covariates were analyzed using the Cox proportional hazards regression model. All statistical analyses were performed using IBM SPSS Statistics V.20, GraphPad Prism V.7, and R V.4.2.1. A two-tailed value of p<0.05 was considered statistically significant in our study.

RESULTS

HA deposition and matrix remodeling define therapy-resistant metastases

Patients enrolled in our study were listed in online supplemental table S1. Representative images of laparoscopic and radiologic evaluation of these cases before and after chemotherapy in therapy-resistant ('Resistant') GC and therapy-responsive ('Responsive') GC were shown in figure 1A. Analysis of peritoneal metastases from 14 patients with GC revealed striking ECM remodeling in therapy-resistant lesions. Elastica van Gieson staining and scanning electron microscopy demonstrated dense, highly aligned collagen fibers in resistant tissues, in contrast to the loose fibrillar structure seen in responsive counterparts (figure 1B). Quantitative morphometry confirmed a markedly greater collagen fiber area and a corresponding reduction in extracellular fibrils (figure 1C). For further investigation of the differences in ECM components, Alcian blue staining was used to show a dramatic enrichment of HA compared with therapy-responsive nodules (figure 1D,E). Consistently, IHC revealed pronounced upregulation of collagen I, and unchanged collagen III and fibronectin expression in resistant lesions (figure 1D,E). An alluvial plot linked HA-high status to therapeutic non-response (figure 1F), and patients with HA-rich metastases exhibited significantly shorter survival (figure 1G). Together, these data identified HA accumulation and ECM stiffening as hallmarks of therapy-resistant peritoneal metastases.

HA-rich metastases display distinct immune-stromal ecosystems

To define the immune landscape, we performed scRNA-seq on 11 peritoneal metastases classified by HA content (HA-high and HA-low). UMAP embedding revealed six major populations: T cells, NK cells, myeloid cells, B cells, stromal fibroblasts, and epithelial cells (figure 2A). HA-high lesions were characterized by an expansion of T cells and stromal cells, accompanied by a marked decline in myeloid cells (figure 2B,C). Spearman correlation analyses confirmed strong positive associations between HA intensity and both T cell (R=0.885) and stromal abundance (figure 2D). Previously, it was reported that stromal cells are correlated with HA accumulation;[37] thus, we focused on T cells in PM tissues. UMAP visualization of T cell clusters subtyped into 20 discrete subsets (0–19) in HA-high (left) and HA-low (right) conditions. According to the dot plot shown in online supplemental figure S1A, several T cell functional subsets were annotated (figure 2E,F). In the 'HA-high' group, there were more $CD8^+$ exhausted T cells, Tregs, and fewer $CD8^+$ CTL cells (figure 2E,F). In addition, HA intensity correlated positively with $CD44^+$ Treg abundance (Spearman r=0.726, p<0.001) and negatively with $CD8^+$ CTLs (r=–0.43, p<0.001) (online supplemental figure S1B,C). For spatial validation, we performed mIHC on a subset of samples (n=5 per group), staining for CD44, CD4, FOXP3, and CD8. Consistent with our scRNA-seq findings, $CD44^+FOXP3^+$ Tregs preferentially localized within HA-rich regions, whereas $CD8^+$ T cells showed relative exclusion (online supplemental figure S1D,E). Next, we checked the expression of the hyaluronan receptor genes. CD44 and ICAM1 are significantly upregulated in HA-high T cells, while LYVE1 was higher in HA-low T cells (figure 2G). Furthermore, the T cell UMAP plot highlighted CD44 enrichment in Tregs (circled) under HA-high and in CD8 CTLs (circled) under HA-low environments (figure 2H). These data suggested that in PM tissues, HA may affect the establishment of a different microenvironment via CD44 stimulation.

HA deposition and degradation mechanisms

To determine the cellular source of HA accumulation, we analyzed scRNA-seq data focusing on HA synthases and HA-degrading enzymes, primarily hyaluronidases (HYAL). Unexpectedly, our analysis revealed that differential HA levels between therapy-resistant and therapy-responsive lesions were primarily driven by impaired HA degradation rather than increased synthesis. Specifically, expression of HYAL1 and HYAL2, which encode hyaluronidases responsible for HA catabolism, was significantly reduced in HA-high metastases compared with HA-low lesions (online supplemental figures S2A and S3D–F). Notably, the differential expression of HYAL1 and HYAL2 was predominantly localized to epithelial tumor cells rather than stromal fibroblasts, as demonstrated by feature plots overlaid on epithelial and stromal UMAP projections (online supplemental figures S2B–D and S3A–F). Immunohistochemical validation in patient samples confirmed the inverse relationship between HYAL protein levels and HA accumulation in resistant nodules (online supplemental figure S3E,F). These findings suggested that the decomposition disorder of HA, resulting from reduced tumor-cell-intrinsic HYAL expression and represented a critical mechanism shaping the HA-enriched, immunosuppressive microenvironment in

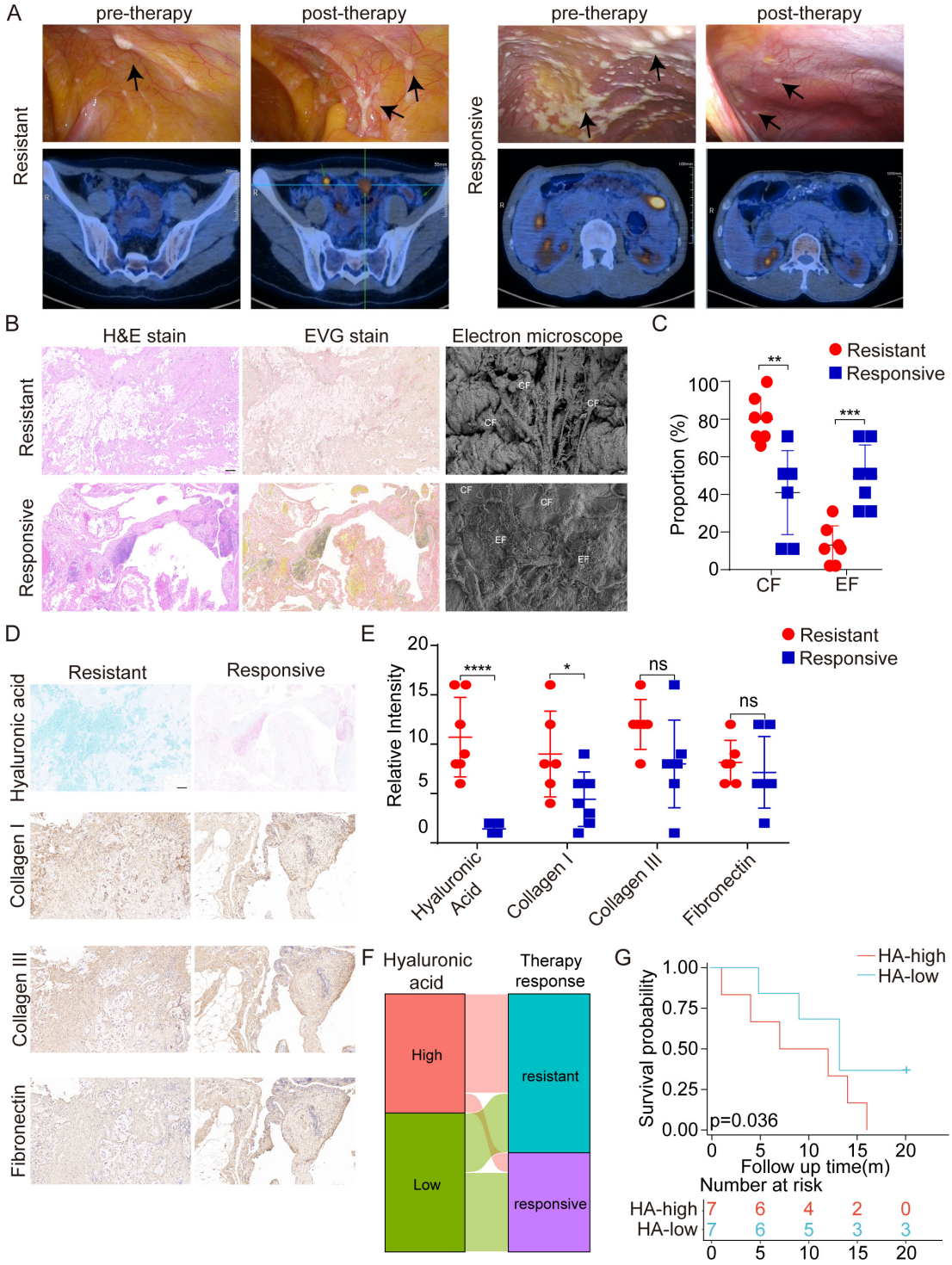

Figure 1 Elevated hyaluronic acid (HA) in peritoneal metastasis correlates with therapy resistance and poor prognosis. (A) Laparoscopic and radiologic evaluation of peritoneal lesions before and after chemotherapy in therapy-resistant ('Resistant') and therapy-responsive ('Responsive') patients with GC. Top panels: Laparoscopic images show scattered peritoneal nodules (black arrows) in cases. Bottom panels: Corresponding axial PET–CT (Positron Emission Tomography and Computed Tomography) images reveal persistently ^{18}F-FDG (Fluorodeoxyglucose)–avid lesions before and after therapy. (B) Histopathological characterization of peritoneal tumor nodules using H&E, Elastica van Gieson (EVG) staining, and scanning electron microscopy (SEM). Scale bars: H&E and EVG, 100 µm; SEM, 10 µm. (C) Quantitative analysis of CF (collagen fibers) and EF (elastic fibers) area fractions in B. (D) Representative alcian blue staining for HA and immunohistochemical detection of collagen I, collagen III, and fibronectin in Resistant and Responsive peritoneal lesions. Scale bars, 50 µm. (E) Semiquantitative scoring of HA, collagen I, collagen III, and fibronectin staining intensities in Resistant (red circles) and Responsive (blue squares) lesions. (F) Alluvial diagram illustrating the association between HA level ('High' vs 'Low') and clinical response to therapy ('Resistant' vs 'Responsive'). (G) Kaplan–Meier survival analysis stratified by HA level in peritoneal metastases. Data represent mean±SD from five independent patient samples per group. *p<0.05, **p<0.01, ***p<0.001, ****p<0.0001, ns, not significant.

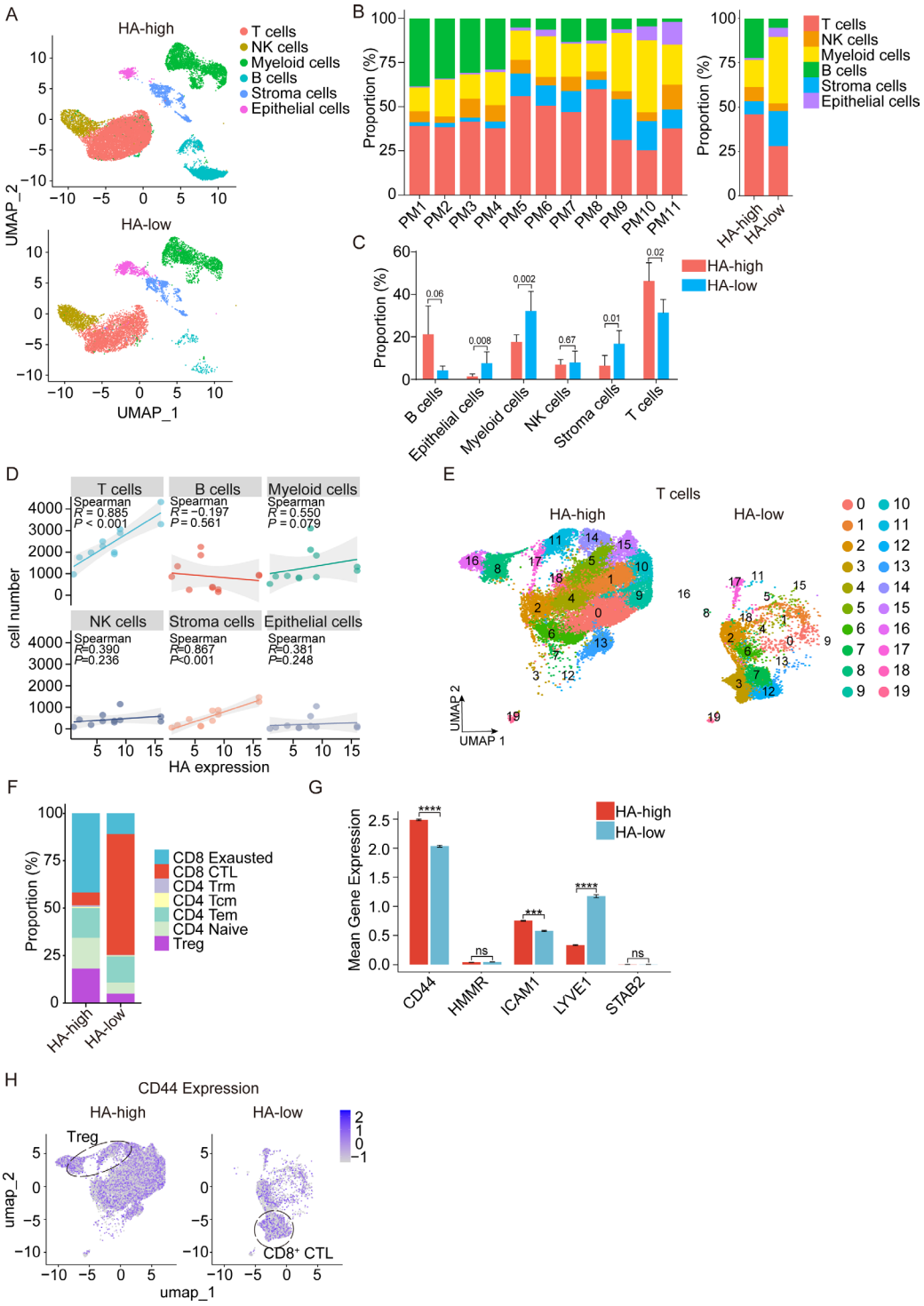

Figure 2 Hyaluronic acid (HA) level correlates with immune landscape remodeling and CD44-associated T cell subset enrichment in peritoneal metastases. (A) UMAP embedding of single-cell transcriptomes from HA-high (top) and HA-low (bottom) peritoneal metastases. (B) Left: Stacked bar charts depicting the proportion of each cell lineage in individual patient samples PM1–PM11. Right: Aggregate comparison of lineage proportions between the HA-high and HA-low groups. (C) Quantification of lineage proportions in HA-high (red) versus HA-low (blue) lesions. Error bars represent mean±SD; unpaired t-tests. (D) Correlation analysis between HA staining intensity and absolute cell numbers for each lineage across all samples. Spearman correlation coefficients (R) and p values are indicated for each cell type. (E) UMAP visualization of T cell clusters subtyped into 20 discrete subsets (0–19) in HA-high (left) and HA-low (right) conditions. (F) Stacked bar chart showing the percentage of T cell functional subsets in HA-high and HA-low groups. (G) Mean normalized expression of hyaluronan receptor genes CD44, HMMR, ICAM1, LYVE1, and STAB2 in T cells from HA-high (red) and HA-low (blue) samples. Error bars denote mean±SD; unpaired t-tests. (H) Feature plots overlaying CD44 expression onto T cell UMAPs for HA-high (left) and HA-low (right) conditions, highlighting CD44 enrichment in regulatory T cells (Tregs) (circled) under HA-high and in CD8 CTL (circled) under HA-low environments. ***p<0.001, ****p<0.0001, ns, not significant.

therapy-resistant peritoneal metastases. This observation was consistent with previous studies demonstrating that tumorous HA accumulation correlated with decreased hyaluronidase activity and confers poor prognostic significance.

CD44$^+$CD4$^+$ T leukocytes specifically enriched in HA-high lesions with poor prognosis

Given the role of CD44 as the principal HA receptor, we sought to find the cell type that mainly expressed CD44 in PM tissues. We mapped CD44 and CD45 on dissociated metastatic cells by t-Distributed Stochastic Neighbor Embedding (t-SNE). HA-high samples displayed a discrete CD44$^+$CD45$^+$ cluster absent in HA-low lesions (figure 3A). Flow cytometry confirmed significantly higher CD44$^+$CD45$^+$ cell frequencies in HA-high nodules (figure 3B,C). Within CD44$^+$ cells, CD45 colocalization dominated, whereas coexpression with CD133, CD326/CK, or vimentin was negligible (figure 3D). Similar enrichment of CD44$^+$CD45$^+$ cells was observed in HA-high omental metastases (online supplemental figure S4A–D), confirming consistency across peritoneal and omental sites, whereas no significant difference was found in ascitic cells (online supplemental figure S4E,F). To delineate the lineage of CD44$^+$CD45$^+$ cells, we gated out CD68$^+$ macrophages and CD56$^+$ NK cells, then identified T cells (CD3$^+$) (figure 3E). In HA-high metastases, 76.3%±6.5% of CD44$^+$CD45$^+$ cells were CD3$^+$ T cells, compared with 57.4%±5.8% in HA-low metastases ($p<0.05$). Among these, CD4$^+$ T cells predominated (45.6%±4.2% vs 20.2%±3.1%, $p<0.01$), with minor contributions from CD8$^+$ T cells and macrophages (figure 3F). Flow histograms revealed FOXP3 expression enriched in CD44$^+$CD45$^+$CD4$^+$ cells from HA-high samples (figure 3G,H). To more comprehensively characterize the CD44$^+$CD4$^+$ population as bona fide Tregs, we performed extended flow cytometry analysis including markers of Treg identity and activation status. CD44$^+$CD4$^+$ T cells from HA-high lesions coexpressed CD25 and FOXP3 in approximately 13.5% of the CD44$^+$CD4$^+$ population, and notably, ~90% of these CD25$^+$FOXP3$^+$ cells demonstrated CD127 low expression, a canonical marker of suppressive Tregs with reduced IL-7 receptor signaling (online supplemental figure S4I-K).[38] Additionally, CD45 isoform analysis revealed that virtually all CD44$^+$CD4$^+$ T cells from HA-high metastases displayed a CD45RO$^+$CD45RA– memory/activated phenotype, consistent with their expected immunomodulatory function within the tumor microenvironment (online supplemental figure S4G,H). These results identify the CD44$^+$CD45$^+$ population as predominantly CD4$^+$ T cells, especially FOXP3$^+$ Tregs in HA-high metastases.

To further validate the prognostic role of CD44$^+$ CD4$^+$ T cells as well as Tregs, a cohort consisting of 141 patients with PM was analyzed (online supplemental figure S5A–D). The baseline data of these 141 patients are shown in online supplemental table S5. The 'CD44-high' group included more male patients, and patients in the 'CD44-high' group had a lower level of serum albumin, indicating a poorer nutritional status, and a higher level of CA72-4. These patients were divided into two groups according to the HA status (the mean value and 95% CI) which are shown in online supplemental figure S5F. In the validation set, higher numbers of HA status were associated with worse OS of patients with GC (online supplemental figure S5E). Furthermore, multivariate Cox regression analysis showed that the number of CD44$^+$CD4$^+$FOXP3$^+$ cells and HA status were independent hazard risk factors ($p<0.0001$; online supplemental figure S5F).

To determine whether the HA-CD44-Treg axis is specific to peritoneal dissemination, we examined CD44$^+$CD4$^+$ T cell infiltration in matched primary GACs from the same patients with peritoneal metastases (online supplemental figure S6A). Notably, no significant difference in CD44$^+$CD4$^+$ T cell abundance was detected between HA-high and HA-low primary tumors (online supplemental figure S6B), indicating that the HA-driven CD44$^+$ Treg enrichment is a metastasis-specific adaptation rather than an intrinsic feature of the primary tumor biology.

HA-CD44 signaling drives Treg polarization and suppressive function in vitro

To delineate the heterogeneity and functional states of CD4$^+$ T cells in the GC peritoneal metastatic microenvironment, we performed scRNA-seq on all the CD4$^+$ T cells isolated from peritoneal metastases. Unbiased clustering of the immune landscape revealed distinct cellular compositions, with a notably higher infiltration of CD4$^+$ T cells in the 'CD44-high' group compared with 'CD44-low' group (online supplemental figure S7A), suggesting a potential correlation between CD4$^+$ T cell abundance and metastatic phenotype. Subsequent in-depth analysis of the CD4$^+$ T cell compartment identified multiple distinct subsets, including naive T cells, central memory T cells, effector memory T cells, T follicular helper-like cells, and Tregs. Comparative analysis between the metastases revealed significant differences in the proportions of these CD4$^+$ T cell subtypes. Specifically, Tregs were significantly enriched in 'CD44-high' nodules relative to 'CD44-low' nodules (online supplemental figure S7B,C), implicating Tregs as key players in the immune microenvironment of more aggressive peritoneal lesions. To understand the developmental relationships between these CD4$^+$ T cell subsets in the tumor microenvironment, we performed pseudotime trajectory analysis. Tregs appeared relatively late along this differentiation trajectory (online supplemental figure S7D), which suggested ongoing in situ differentiation or recruitment of Tregs within the peritoneal metastatic niche. Then, examining the gene expression dynamics along this pseudotime trajectory, we observed a progressive upregulation of both CD44 and FOXP3 transcripts (online supplemental figure S7E). The expression of CD44 started increasing in early activated CD4$^+$ T cells and reached its peak in the Tregs cluster, similar to the expression pattern of FOXP3, while central memory T cells (T_{CM} cells) also displayed high CD44 expression, consistent with its established role

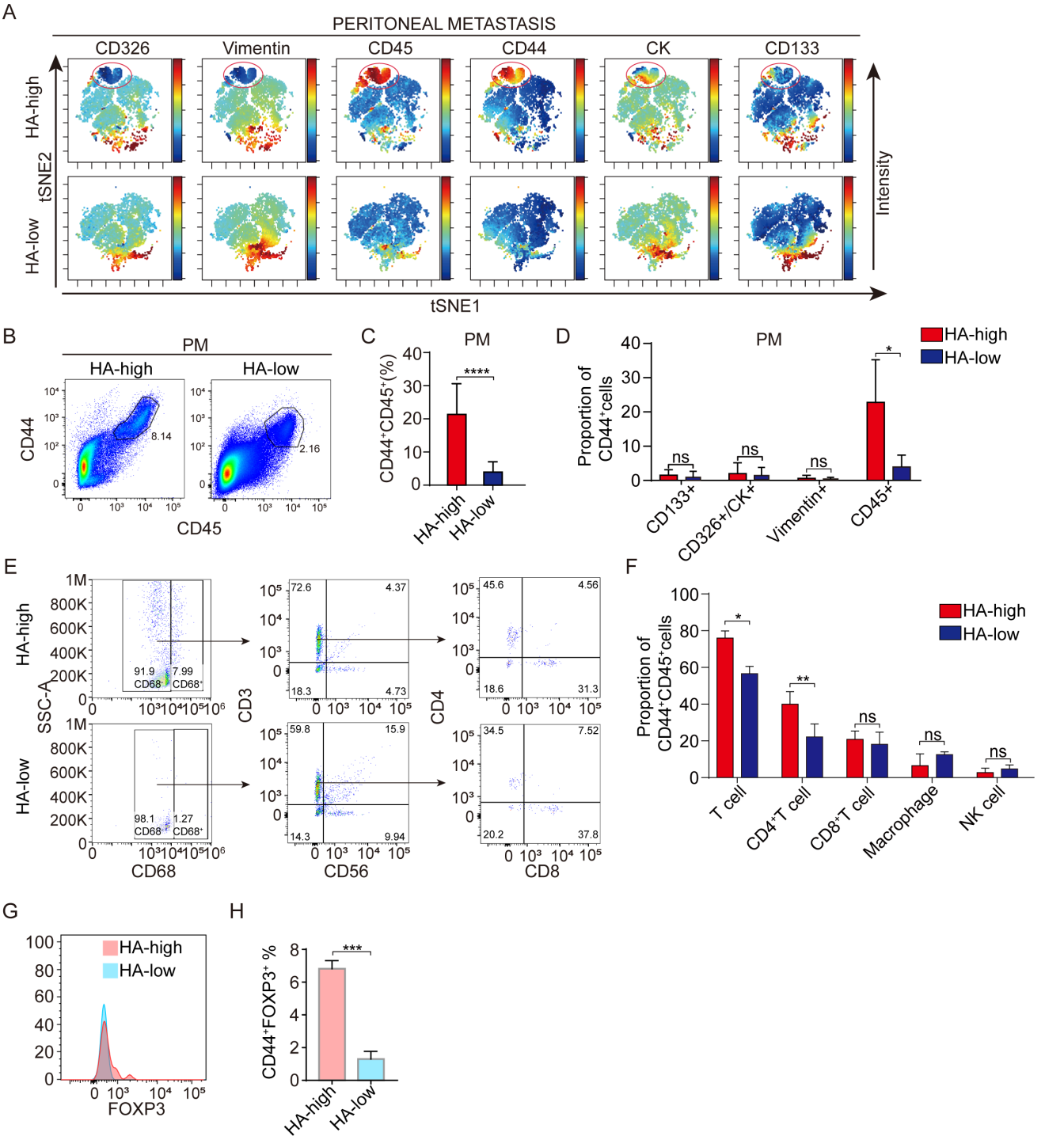

Figure 3 CD44$^+$CD4$^+$ T cells enrich in hyaluronic acid (HA)-high peritoneal metastases and define a Treg niche. (A) v-SNE maps showing expression intensity of CD326, vimentin, CD45, CD44, cytokeratin (CK), and CD133 in single-cell suspensions from HA-high (top row) and HA-low (bottom row) peritoneal metastases. CD45$^+$CD44$^+$ clusters (circled) are prominent only in HA-high samples. Color bars denote normalized expression. (B) Representative flow cytometry dot plots gating CD45 versus CD44 in fresh peritoneal metastasis (PM) samples from HA-high and HA-low groups. The percentage of CD44$^+$CD45$^+$ cells is indicated. (C) Quantification of CD44$^+$CD45$^+$ cell frequency in HA-high (red) versus HA-low (blue) metastases (mean±SD; ****p<0.0001, unpaired t-test; n=6 per group). (D) Proportion of CD44$^+$ cells coexpressing CD133, CD326/CK, vimentin, or CD45 in HA-high (red) and HA-low (blue) groups (*p<0.05; ns, not significant). (E) Sequential gating strategy for HA-high (top) and HA-low (bottom) PM samples. Left plots: CD68 versus SSC-A (Side Scatter Area) to exclude macrophages. Middle plots: CD3 versus CD56 to identify T cells and natural killer (NK) cells. Right plots: CD4 versus CD8 within CD3$^+$ cells. (F) Proportion of CD44$^+$CD45$^+$ cells belonging to T cells, CD4$^+$ T cells, CD8$^+$ T cells, macrophages, or NK cells in HA-high (red) versus HA-low (blue) samples. (*p<0.05, **p<0.01). (G) Representative overlaid histograms of FOXP3 expression in CD44$^+$CD45$^+$ T cells from HA-high (red) and HA-low (blue) samples. (H) Quantification of FOXP3$^+$ Treg frequency among CD44$^+$CD45$^+$ cells in HA-high versus HA-low metastases (mean±SD; ***p<0.001; unpaired t-test). Treg, regulatory T cell

as an activation and memory marker. The concomitant maximal expression of both CD44 and FOXP3 in Tregs strongly suggested a functional link between CD44 and the Treg lineage within this specific pathological context.

To validate these observations at the protein level, we performed flow cytometry on immune cells isolated from ascites fluid of patients with GC with PM. Consistent with the scRNA-seq data, CD44 protein expression was significantly higher on Tregs compared with other $CD4^+$ T cell subsets (figure 4A). This confirmed the preferential high-level expression of CD44 on Tregs in the human GC peritoneal microenvironment. Purified human Tregs were stimulated in vitro with HA and a specific CD44 agonist Angstrom6. Both HA and Angstrom6 significantly enhanced Treg proliferation as measured by CCK8 assay (online supplemental figure S8A). Conversely, blockade of CD44 signaling using the neutralizing anti-CD44 antibody markedly inhibited their proliferative capacity (online supplemental figure S8A), indicating that CD44 signaling is critical for Treg expansion. In addition, stimulation or blockade of CD44 did not influence the apoptosis of $CD4^+$ T cells (online supplemental figure S8B). Interestingly, CD44 blockade mainly restricted T cells' proliferation in both $CD4^+$ and $CD8^+$ T cells (online supplemental figure S8C–F). Then, we tested whether HA engagement of CD44 induces human Treg differentiation. To confirm the specificity of HA-mediated effects and exclude non-specific inflammatory activation, we performed comprehensive mechanistic controls. The HA polymer used in these studies (molecular weight 800–1500 kDa; MCE HY-B0633A) was selected based on previous evidence that high-molecular-weight HA preferentially engages CD44 receptor signaling rather than activating pattern-recognition receptors such as Toll-like receptor 2 (TLR2) and Toll-like receptor 4 (TLR4), which are typically triggered by low-molecular-weight HA fragments (<10 kDa). Additionally, the HA preparation was confirmed to be endotoxin-free (LAL assay: <0.1 EU/mg), excluding TLR4-mediated confounding effects. Naïve $CD4^+$ T cells stimulated with HA plus IL-2/TGF-β and CD3/CD28 exhibited a threefold increase in $CD44^+FOXP3^+$ Tregs, and anti-CD44 blocking antibody reduced Treg induction (figure 4B,C). To directly demonstrate HA specificity, we pretreated HA with bovine testicular hyaluronidase (100 U/mL, 37°C, 2 hours) to enzymatically degrade HA into small fragments, then assessed its capacity to induce $FOXP3^+$ Treg differentiation. Hyaluronidase-digested HA failed to promote Treg induction, confirming that the biological effect requires intact, high-molecular-weight HA and it was mediated specifically through CD44 signaling rather than non-specific inflammatory pathways (online supplemental figure S8G,H). Co-culture of conditioned $CD4^+$ cells with autologous $CD8^+$ T cells (figure 4D) showed HA-treated $CD4^+$ cells suppressed $CD8^+$ GZMB and IFN-γ production, whereas CD44 blockade restored effector cytokine expression (figure 4E–G). ELISA of culture supernatants confirmed HA increased IL-10 and TGF-β secretion, both reversed by αCD44 (figure 4H,I). Besides, to clarify whether HA-stimulated $CD4^+$ T cell-mediated suppression of $CD8^+$ T cells operates through contact-dependent or soluble-factor mechanisms, we performed Transwell co-culture experiments separating HA-treated $CD4^+$ T cells from autologous $CD8^+$ T cells by a 0.4 µm membrane. Partial maintenance of $CD8^+$ T cell suppression across the Transwell partition indicated that both soluble mediators and direct cell-cell contact contributed to the suppressive phenotype. Cytokine-neutralization assays using blocking antibodies against IL-10 and TGF-β (online supplemental figure S8I,J) confirmed the roles of these soluble immunosuppressive factors in the HA-CD44-mediated Treg-dependent suppression of $CD8^+$ effector function. These data demonstrated the HA-CD44 axis as a potent driver of Treg differentiation and immunosuppressive function.

$CD44^+CD4^+$ T cells promote PM in vivo

CD44 and CD4 expression were checked in patient-derived PC-04 cells (figure 5A,B). To evaluate the pro-metastatic role of $CD44^+CD4^+$ cells, humanized NSG mice were injected intraperitoneally with patient-derived PC-04 cells either unsorted, $CD44^+CD4^+$-depleted, or $CD44^+CD4^+$-enriched (figure 5C). Mice lacking $CD44^+CD4^+$ cells developed significantly fewer nodules and lower nodule weight (figure 5D–F). $CD44^+CD4^+$ depletion extended median survival beyond 50 days versus 27 days in controls (figure 5G). In the syngeneic YTN16 model (figure 5H), anti-CD44 treatment markedly reduced metastases and prolonged survival (figure 5I–M). Besides, CD44 blockade definitely reduced the amount of $CD44^+CD4^+$ T cells in abdominal metastases (online supplemental figure S9A,B). To mechanistically demonstrate that anti-CD44 blockade reduces peritoneal metastatic burden through immune modulation rather than direct tumor cytotoxicity (online supplemental figure S9C), we performed comprehensive flow cytometric analysis of peritoneal tissues harvested from treated and control mice. In the immunocompetent syngeneic YTN16 model, anti-CD44 treatment significantly reduced $CD4^+FOXP3^+$ Treg infiltration in peritoneal metastatic lesions and simultaneously increased $CD8^+$ T cell frequency, whereas macrophage abundance remained unchanged (online supplemental figure S9D–F).

To exclude the possibility that the therapeutic benefit of anti-CD44 blockade results from direct inhibition of tumor cell adhesion or migration, we performed in vitro assays using PC-04 cells treated with anti-CD44 antibody. While anti-CD44 treatment dose-dependently reduced tumor cell viability at higher concentrations (5 µg/mL and 10 µg/mL; online supplemental figure S10A), treatment did not impair the capacity of GC cells to migrate across and penetrate a confluent human peritoneal mesothelial cell monolayer (online supplemental figure S10B,C). This dissociation between modest direct tumor effects and the substantial therapeutic benefits observed in vivo underscored that anti-CD44 therapy primarily operated through immune modulation. Furthermore, the

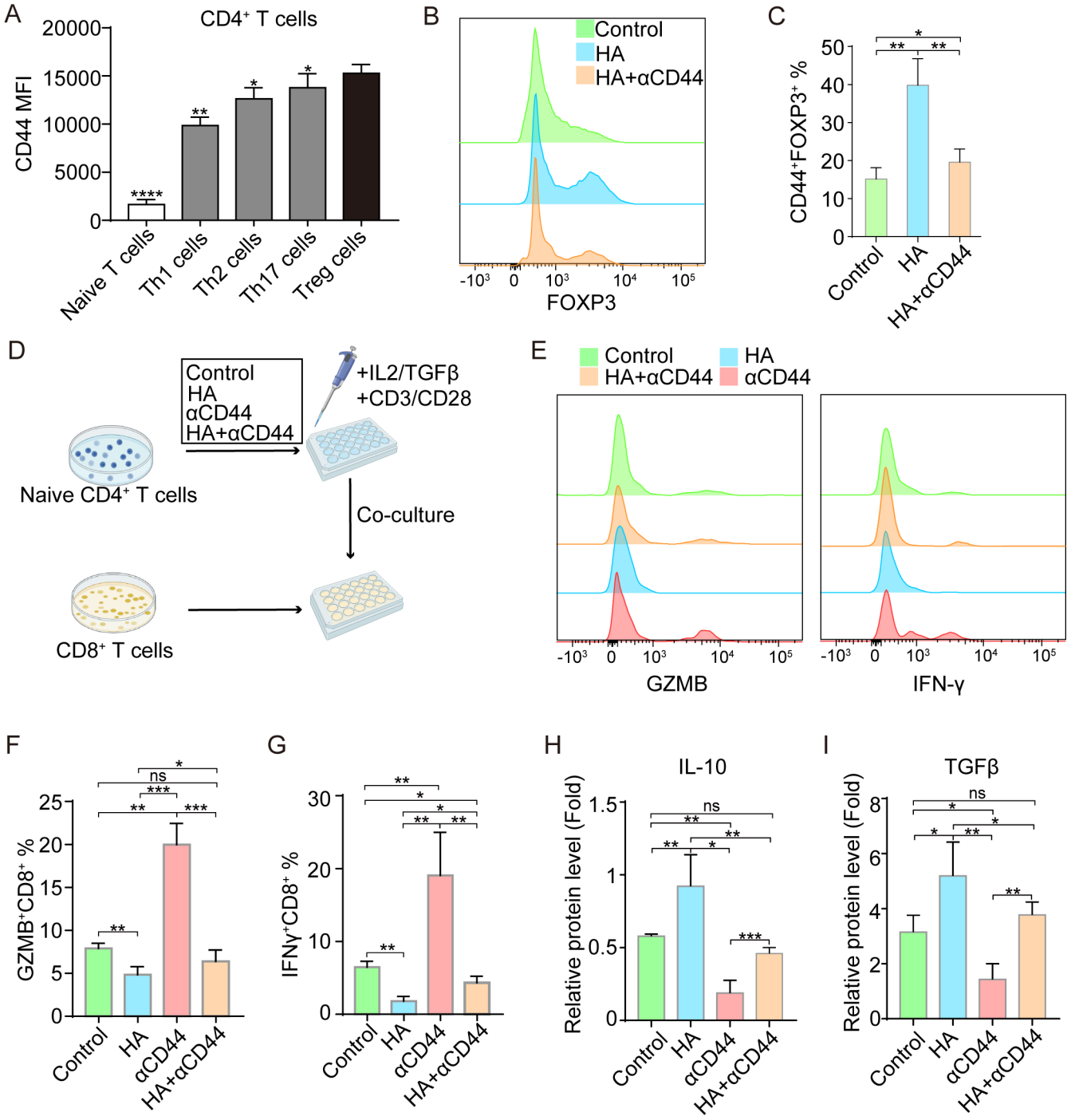

Figure 4 CD44 engagement by hyaluronic acid (HA) enhances Treg differentiation and suppresses cytotoxic T cell function in vitro. (A) Surface CD44 mean fluorescence intensity (MFI) measured by flow cytometry on purified human CD4⁺ T cell subsets: naïve, T helper cells (Th1), Th2, Th17, and Tregs after 48 hours stimulation. (****p<0.0001, **p<0.01, *p<0.05; t test). (B) Representative flow cytometry histograms of FOXP3 expression in CD4⁺ naïve T cells after 5-day culture with control medium (green), HA (blue), or HA plus anti-CD44 blocking antibody (HA + αCD44, orange). (C) Quantification of CD44⁺FOXP3⁺ Treg generation (% of CD4⁺ cells) under control, HA, and HA + αCD44 conditions (mean±SD; **p < 0.01, *p < 0.05; t test). (D) Schematic of co-culture assay where naïve CD4⁺ T cells are pretreated with HA, αCD44, or both, in the presence of IL-2/TGF-β and CD3/CD28 stimulation, then co-cultured with autologous CD8⁺ T cells. (E) Representative histograms of granzyme B (GZMB) and IFN-γ expression in CD8⁺ T cells after 72 hours co-culture with CD4⁺ T cells pretreated as in (D): control (green), HA (blue), HA + αCD44 (orange), or αCD44 alone (red). (F–G) Quantification of GZMB⁺ (F) and IFN-γ⁺ (G) CD8⁺ T cells from co-culture assay (mean±SD; ns, not significant; *p<0.05, **p<0.01, ***p<0.001; t test). HA-treated CD4⁺ cells suppress CD8⁺ effector function, which is reversed by CD44 blockade. (H,I) ELISA measurement of immunosuppressive cytokines IL-10 (H) and TGF-β (I) in culture supernatants from co-cultures described in (D). (mean fold change±SD; *p<0.05, **p<0.01, ***p<0.001; t test). Treg, regulatory T cell.

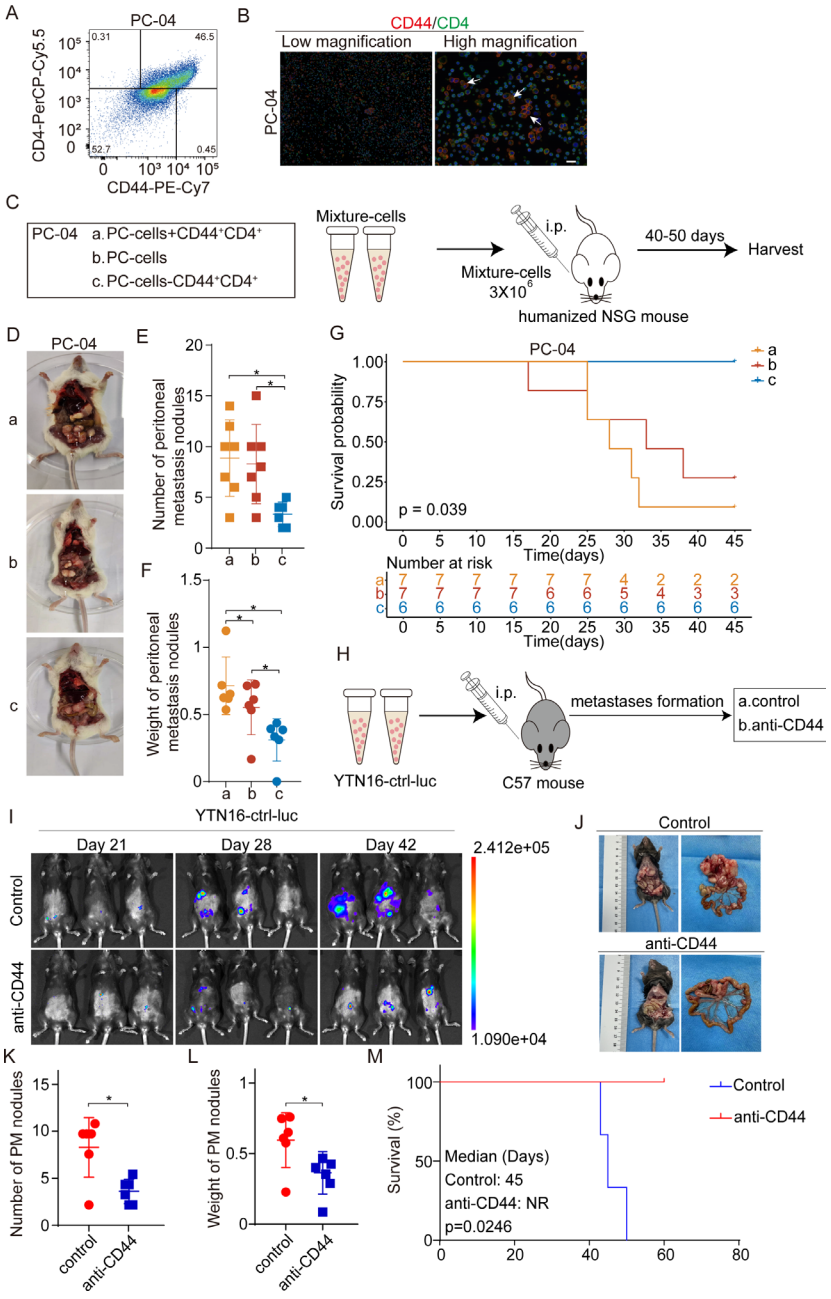

Figure 5 CD44$^+$CD4$^+$ T cells drive peritoneal metastasis (PM) formation, and targeting CD44 prolongs survival in mouse models.(A) Flow cytometry of peritoneal lavage cells harvested from one hyaluronic acid (HA)-high patient (PC-04) showing gating for CD4$^+$PerCP-Cy5.5 versus CD44-PE-Cy7. Percentage of CD4$^+$CD44$^+$ T cells is indicated in the upper right quadrant. (B) Immunofluorescence staining of peritoneal metastasis sections from PC-04 demonstrating colocalization of CD44 (red) and CD4 (green). Left: low-magnification overview. Right: high-magnification inset showing CD44$^+$CD4$^+$ cells (white arrows). Nuclei counterstained with DAPI (blue). Scale bar=50 µm. (C) Schematic of the peritoneal xenograft experiment. Humanized NSG mice with human PBMC encrafted were injected intraperitoneally with 3×10^6 cells comprising (a) unsorted PC-04 tumor cells, (b) PC-04 cells alone, or (c) PC-04 cells depleted of CD44$^+$CD4$^+$ T cells. Mice were monitored for 40–50 days postinjection. (D) Representative necropsy images of the peritoneal cavity at endpoint for groups (a–c). (E,F) Quantification of peritoneal metastasis nodule number (E) and total nodule weight (F) in groups (a–c). (*p<0.05; unpaired t-test; n=6 per group). (G) Kaplan–Meier survival curves of NSG mice from groups (a–c). (H) Schematic of the syngeneic peritoneal metastasis experiment. C57BL/6 mice received intraperitoneal injection of YTN16-ctrl-luc cells, followed by treatment with control IgG (a) or anti-CD44 antibody (b). (I) Bioluminescence imaging of YTN16-ctrl-luc peritoneal metastases on days 21, 28, and 42 postinjection in control and anti-CD44–treated mice. Color scale indicates photon flux (photons/s/cm^2). (J) Representative photos of peritoneal metastasis nodules harvested at endpoint from control and anti-CD44–treated mice. (K,L) Quantification of peritoneal metastasis nodule number (K) and weight (L) in control versus anti-CD44 treated mice. (*p<0.05; unpaired t-test; n=5 per group). (M) Kaplan–Meier survival analysis of YTN16-ctrl-luc–bearing mice treated with control IgG (blue) or anti-CD44 (red). Anti-CD44 significantly prolongs survival (median not reached vs 45 days; p=0.0246, log-rank test). All data represent mean±SD. PBMC, peripheral blood mononuclear cell.

peritoneal metastatic niche was characterized by a sparse distribution of cancer cells embedded within abundant stromal and immune cell populations, rendering direct tumor-targeting effects less dominant than immune-mediated mechanisms.

CD44–IQGAP1 interaction activates RAC1–SMAD3–FOXP3 axis

To explore the intracellular regulation of CD44 that regulates Treg differentiation, we collected the $CD4^+$ T cells from ascites of patients with GC PM, CD44 protein was pulled down and mass spectrum analysis was carried out to analyze the protein precipitation. Proteomic ranking placed CD44, IQGAP1, and RAC1 among the top 1% most abundant proteins (figure 6A). Confocal imaging showed CD44-IQGAP1 colocalization at the plasma membrane, disrupted by anti-CD44 (figure 6B). Additionally, we verified the endogenous binding relationship between IQGAP1 and CD44 proteins in Tregs (figure 6C,D). In vitro immunoprecipitation assays indicated that CD44 interacted with wild type IQGAP1. In addition, RAC1 was reported to be one of the downstream signaling molecules that directly interacted with IQGAP1; thus, RAC1 was also detected, and it interacted with the CD44/IQGAP1 complex as expected. To validate whether the interacting domain of CD44 is the intracellular domain, different deletions of Flag-labeled CD44 and MYC-IQGAP1 were examined (figure 6E,F). We observed that the total CD44 interacted with IQGAP1 while the intracellular-deleted domain (amino acids 21–670) did not mediate the interaction between these two proteins (figure 6F). To explore the function of the CD44/IQGAP1/RAC1 complex in Treg differentiation, $CD4^+$ naïve T cells were pretreated with anti-CD44 antibody, IQGAP1 inhibitor UR778Br, and RAC1 inhibitor NSC23766 trihydrochloride. Flow cytometry was conducted so that all the three chemicals restrained the induction of Tregs (figure 6G,H). Furthermore, as the TGFβ signaling pathway is the classical approach for Treg differentiation,[39] we investigated if HA-CD44 induced Smad3 phosphorylation. HA stimulation of FLAG-CD44-expressing cells induced SMAD3 phosphorylation, abrogated by αCD44, IQGAP1 inhibitor UR778Br, or RAC1 inhibitor NSC23766 (figure 6I–K). TGF-β receptor inhibition similarly blocked pSMAD3 (figure 6L). UR778Br or αCD44 reduced IL-10 and TGF-β secretion (figure 6M,N). Overexpression of FLAG-CD44 or MYC-IQGAP1 enhanced foxp3 mRNA and promoter activity, effects reversed by IQGAP1 knockdown or TGF-β receptor blockade (figure 6O–Q).

Targeting CD44 alleviates Treg-mediated immunosuppression and potentiates the efficacy of anti-PD-1 immunotherapy in GC PM

To investigate the potential role of $CD44^+$ Tregs in immunosuppression effect in PM, we explored whether the amount of $CD44^+$ Tregs will influence the effect of immunotherapy. Twelve patients with GC PM who had undergone immunotherapy were selected (online supplemental table S6), and as expected, patients who were 'partial response' (PR) had a better survival rate than those who were 'stable disease/progressive disease' (SD/PD) (figure 7A). Among them, patients with PR had a lower percentage of $CD44^+$ Tregs, $PD1^+$ cells, and a higher percentage of $CD8^+$ cells (figure 7B–E). To further investigate if the combination of anti-CD44 and anti-PD1 would alleviate Treg-mediated immunosuppression, C57 mice were randomized into four cohorts receiving different treatments mentioned in figure 7F. Tumor growth was monitored at various time points (online supplemental figure S11A). Interestingly, the combination of anti-CD44 and anti-PD1 reduced the number of tumor nodes in mice abdomen (figure 7F–H), accompanied by the reduced amount of $CD4^+$ T cells including Tregs, $PD1^+$ cells, and the induction of $CD8^+$ cells (figure 7I, (online supplemental figure S11B). In conclusion, combined anti-CD44 and anti-PD-1 treatment demonstrated enhanced therapeutic efficacy compared with either monotherapy. Finally, integration of these findings into a mechanistic schematic illustrated that HA engagement of CD44 recruits IQGAP1 and activates RAC1, which in turn phosphorylates SMAD3 to drive FOXP3 transcription and Treg differentiation, thereby fostering immune suppression and PM (figure 7J).

DISCUSSION

The understanding of GC at the cellular and molecular levels has advanced in recent years.[40 41] Metastatic GC cells in the peritoneum have a unique gene expression, and mutational and copy-number alteration profile, indicating extensive intertumoral and intratumoral heterogeneity, which is associated with drug resistance and poor OS.[42] However, there has been limited progress in clinical treatment due to the 'unresectable' characteristic of PM.[43] Inadequate specimens obtained via endoscopic biopsy also hinder the understanding of GC intratumoral heterogeneity.[44] Thus, the biology of GC PM remains largely understudied. Recently, the study of metastatic GC has been facilitated by the development of malignant ascites-derived cell lines and organoids,[42 45–47] as well as the increasing frequency of laparoscopic exploration and Hyperthermic Intraperitoneal Chemotherapy (HIPEC) treatment.[48 49] Technological advances, including single-cell transcriptomic and proteomic analyses, have revealed novel cellular subtypes and gene prognostic signatures.[50] In this study, we focused on the immunobiology of GC peritoneal metastatic lesions that related to tumor therapy.

Previous prospective studies have suggested that HA deposition on tumor cells promote peritoneal adhesion, extravasation, and metastatic colonization mainly by creating adhesive niches and altering stromal mechanics.[9 37] In our study, we show that HA plays an active immunoregulatory role beyond

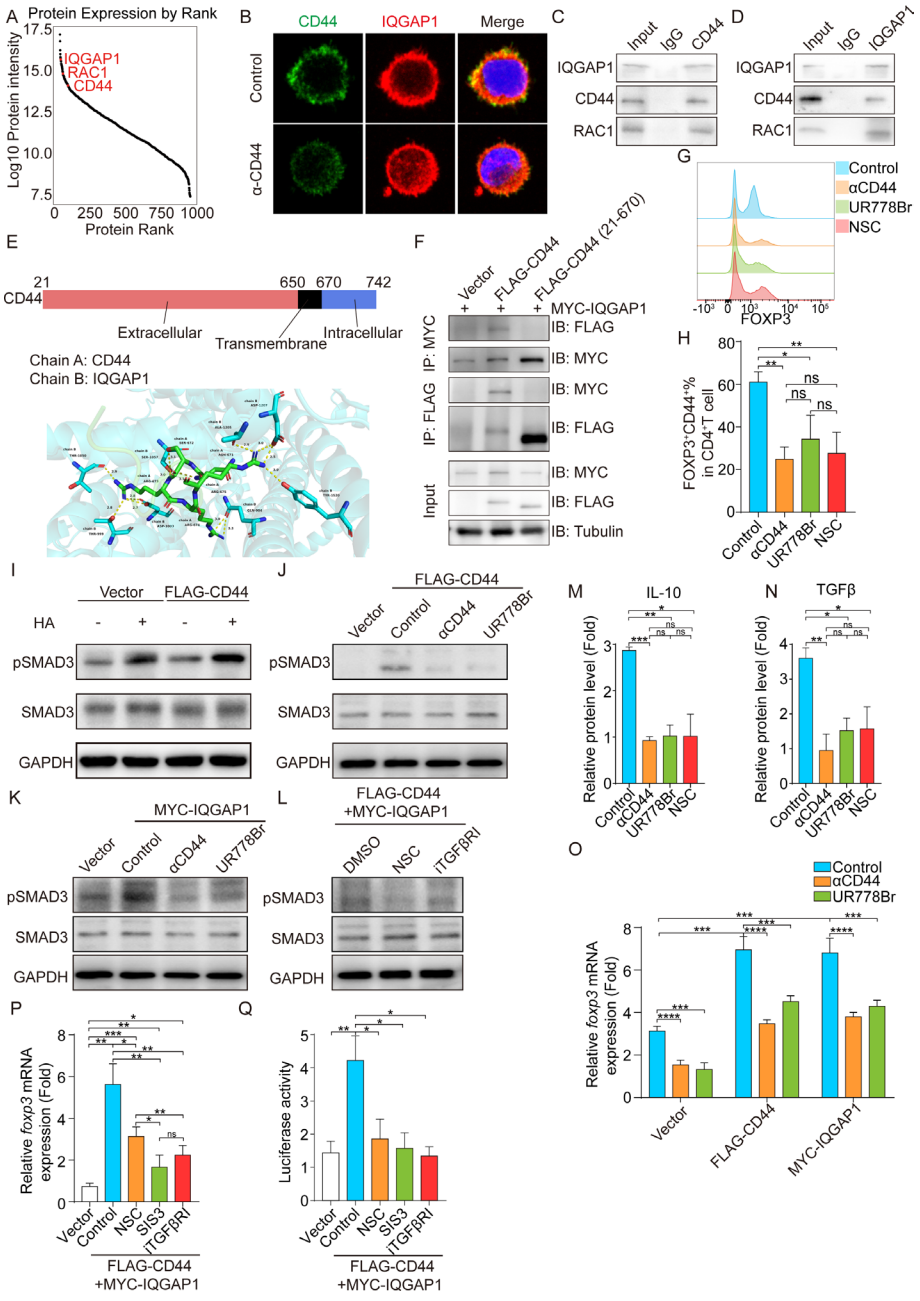

Figure 6 CD44 physically interacts with IQGAP1 to activate RAC1–SMAD3 signaling and FOXP3 transcription.(A) Rank-ordered abundance of proteins identified by mass spectrometry in CD44$^+$ Tregs lysate. CD44, IQGAP1, and RAC1 (red labels) rank among the top 1% of detected proteins. (B) Confocal immunofluorescence of control or anti-CD44 treated CD44$^+$ Tregs stained for CD44 (green) and IQGAP1 (red). Merge panels (right) include DAPI (blue). Scale bar=10 µm. (C,D) Co-immunoprecipitation of CD44 and IQGAP1 from cell lysates. Input and IgG controls are shown. (E) Schematic of CD44 domain architecture (amino acids 21–742) with extracellular (red), transmembrane (black), and intracellular (blue) regions (top), and molecular docking model depicting interaction interface between CD44 extracellular domain and IQGAP1 (bottom). Key interacting residues are highlighted. (F) Co-IP in CD44$^+$ Tregs transfected with FLAG-CD44 full-length or FLAG-CD44 (21–670) truncation and MYC-IQGAP1. Tubulin serves as loading control. (G–H) In vitro Treg induction assay measuring FOXP3 expression in CD4$^+$ T cells stimulated in the presence of control, anti-CD44, UR778Br (IQGAP1 inhibitor), or NSC23766 (RAC1 inhibitor). (G) Representative flow cytometry histograms. (H) Quantification of CD44$^+$FOXP3$^+$ T cells (mean±SD; **p<0.01, *p<0.05; t test). (I–L) Western blots assessing SMAD3 phosphorylation in CD44$^+$CD4$^+$ T cells under various perturbations. GAPDH serves as loading control. (M,N) ELISA quantification of IL-10 (M) and TGF-β (N) in conditioned medium from CD4$^+$ T cell cultures under control, αCD44, UR778Br, or NSC23766 treatment (mean fold change±SD; **p<0.01, *p<0.05; t test). (O–Q) FOXP3 transcriptional activation assays. (O) Quantitative real-time PCR (qRT-PCR) of foxp3 mRNA in CD4$^+$ T cells transfected with vector, FLAG-CD44, or MYC-IQGAP1 (mean fold change±SD; ***p<0.001, ****p<0.0001; t test). (P) foxp3 mRNA levels in FLAG-CD44 + MYC-IQGAP1 cells treated with control, NSC23766, SIS3 (smad3 inhibitor) or iTGFβRI (TGFβRI inhibitor) treatment (mean fold change±SD; **p<0.01, *p<0.05; t test). (Q) Luciferase reporter assays of foxp3 promoter activity under same conditions as (P) (mean±SD; **p<0.01, *p<0.05; t test). ns, not significant; Treg, regulatory T cell.

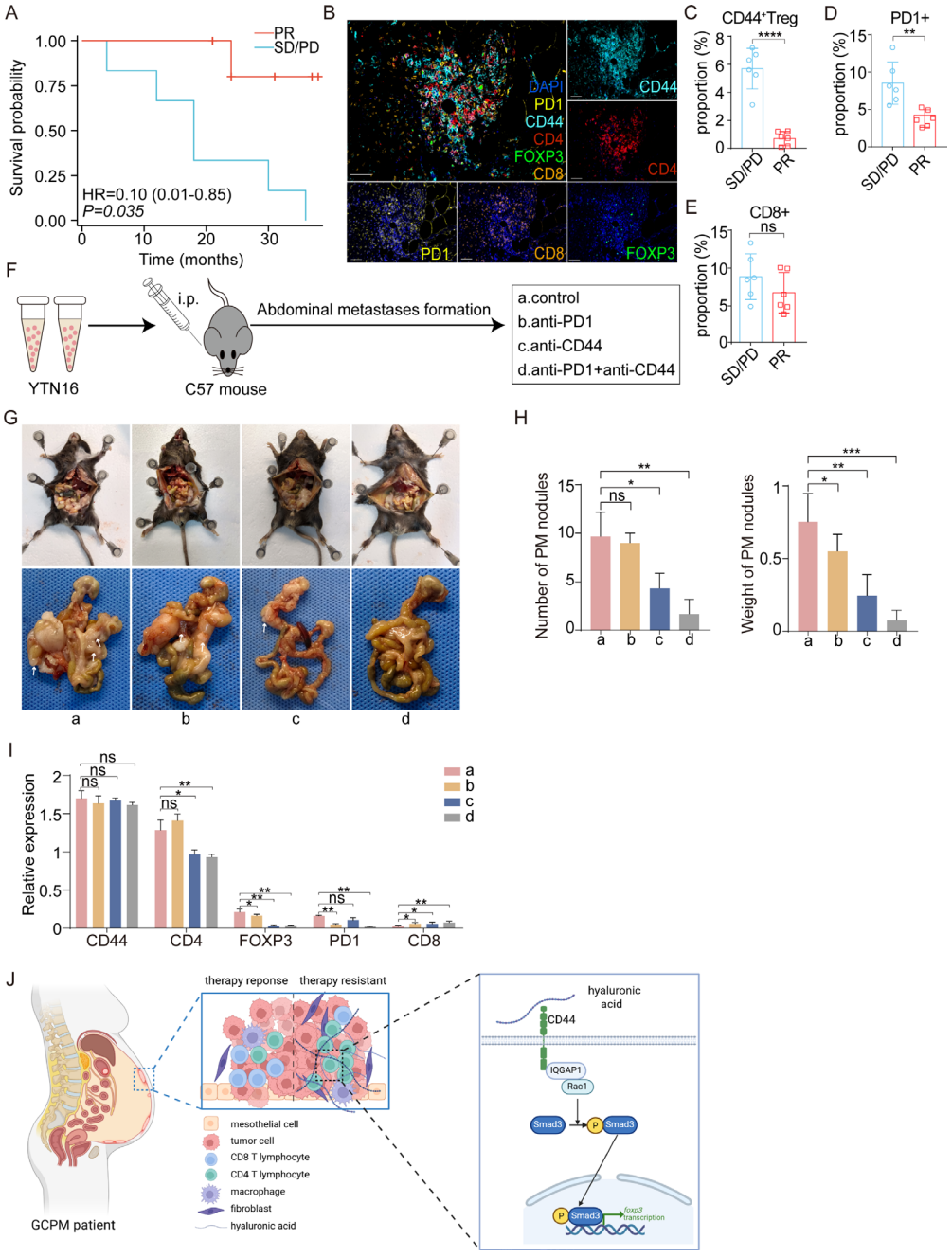

Figure 7 CD44$^+$ Tregs correlate with immunotherapy resistance, and combined CD44/PD-1 blockade enhances therapeutic efficacy in peritoneal metastasis (A) Kaplan-Meier survival analysis of patients with gastric cancer (GC) receiving immunotherapy, stratified by treatment response. Patients achieving partial response (PR, yellow) showed improved survival compared with those with stable/progressive disease (SD/PD, blue). HR=0.21 (95% CI 0.06 to 0.74), log-rank test p=0.075. (B) Representative multiple immunohistochemistry (mIHC) imaging of peritoneal metastatic tissue from patients with GC. Merged image (left) shows spatial distribution of immune markers: DAPI (blue, nuclei), PD1 (yellow), CD4 (red), FOXP3 (green), CD8 (orange), and CD44 (cyan). Individual channel images (right panels) demonstrate CD44, CD4, and FOXP3 expression patterns. Scale bar=50 µm. (C–E) Quantitative analysis of immune cell infiltration in peritoneal metastases from patients with different immunotherapy responses. (F) Experimental design for combination therapy study. YTN16 gastric cancer cells were injected intraperitoneally into C57BL/6 mice, followed by treatment with: (a) control, (b) anti-PD1, (c) anti-CD44, or (d) anti-PD1 and anti-CD44 combination therapy. (G) Representative image of mice corpse and peritoneal metastases at the endpoint. Upper panels show in situ peritoneal tumors; lower panels show excised tumor nodules. (H) Quantification of therapeutic efficacy shown in G. (I) Quantification of CD44, CD4, FOXP3, PD-1, and CD8 immunofluorescence intensity in peritoneal tumors from each treatment group normalized to control (a). (J) Schematic model illustrating HA-CD44-IQGAP1-RAC1-SMAD3 signaling cascade in CD4$^+$ T cells: HA engagement of CD44 recruits IQGAP1 and activates RAC1, driving SMAD3 phosphorylation, nuclear translocation, and FOXP3 transcription to promote Treg differentiation and immune suppression in therapy-resistant metastases. Data represent mean±SD; n=3 independent experiments. *p<0.05, **p<0.01, ***p<0.001, ****p<0.0001 and ns, not significant.

serving as a physical barrier. Furthermore, our findings revealed that HA production is mainly about the expression of HYAL family rather than HA synthases. Furthermore, the differential expression of HYAL1 and HYAL2 is primarily within tumor epithelial cells rather than stromal fibroblasts. This observation is consistent with reported tumorous HA accumulation correlating with decreased HYAL1 and HYAL2 protein levels, implicating impaired degradation as a driver of HA buildup in epithelial tumors.[51] Excessive HA engages CD44 on $CD4^+$ T cells and drives their differentiation into Tregs. The accumulation of these $CD44^+$ Tregs establishes a profoundly immunosuppressive niche that restrains cytotoxic T cell activity and possibly confers resistance to chemotherapy, targeted therapy, and immunotherapy. This HA-CD44 axis mechanistically links ECM remodeling to immune evasion and therapeutic failure in PM.

The involvement of CD44 in cancer progression and metastasis is well documented.[52] Previous studies have often focused on CD44 expression on cancer cells themselves, linking it to cancer stem cell properties, chemoresistance, and invasive behavior.[53 54] Furthermore, anti-CD44 therapies are promising candidates for clinical translation, particularly in GC to overcome microenvironment-mediated resistance. In this study, we suggest that CD44-directed therapies truly show the effect in PM treatment due to their impact on $CD44^+CD4^+$ T cells, which extend this understanding by highlighting a vital role for CD44 expressed on immune cells, in shaping the peritoneal metastatic niche. In addition, CD44 may maintain $CD4^+$ T cell stability and promote $CD4^+$ T cells to differentiate into Tregs according to our in vitro studies. The identification of CD44 as a key regulator of Treg differentiation in GC PM has significant implications for our understanding of tumor immunology.

Furthermore, our work delineated the CD44/IQGAP1/RAC1 complex that regulates Smad3 signaling cascade in T cells. The scaffold protein IQGAP1 has emerged as a critical node in various signaling pathways, serving as a platform for the assembly of multiprotein complexes that regulate diverse cellular processes.[55] IQGAP1 interacts with numerous binding partners, including small GTPases such as RAC1, to modulate cytoskeletal dynamics, cell adhesion, and signal transduction.[56] Interestingly, IQGAP1 has been implicated in T cell receptor signaling and immune cell function, suggesting a potential role in regulating T cell responses in the tumor microenvironment.[57 58] The Smad protein is canonically activated by TGF-β signaling to induce FOXP3 expression. A previous study has implied that Galectin-9 increased iTregs stability and function by directly binding to its receptor CD44, which formed a complex with TGFβRI and thus activated Smad3.[39] This mechanism parallels previous observations by Wu *et al* showing that Galectin-9 engages CD44 to form a complex with TGFβR1, augmenting Treg stability. Our findings suggest that HA, as a high-abundance CD44 ligand in the peritoneal metastatic microenvironment, performs a functionally analogous role to Galectin-9, facilitating CD44-TGFβR1 proximity and promoting downstream SMAD3 activation. Thus, CD44 serves as a dynamic signaling hub: when engaged by different extracellular ligands such as HA or Galectin-9, CD44 recruits and stabilizes TGFβR1 through scaffold proteins including IQGAP1 and RAC1, thereby amplifying canonical TGFβ signaling and promoting FOXP3-dependent Treg differentiation. In addition, pharmacological inhibition of TGFβR1 (iTGFβRI) partially abolishes HA-induced SMAD3 phosphorylation, indicating that TGFβR1 kinase activity is one approach for the transcriptional program driving Treg differentiation, while SMAD3 phosphorylation could be induced by RAC1 likely through Mitogen-activated protein kinases (MAPK)-mediated or p21-activated kinases (PAK)-mediated phosphorylation of the SMAD3 linker region.[59] Our current work is focusing on the expression of HA in PM that really arouses our interests and may discover new targets in PM treatment.

In conclusion, our study reveals that excessive HA deposition reshapes the ECM and activates CD44-dependent signaling in $CD4^+$ T cells, driving IQGAP1/RAC1/Smad3-mediated Treg differentiation. This HA-enriched niche impedes cytotoxic T cell function and limits the efficacy of systemic and immune-based therapies. By demonstrating that CD44 blockade restores immune activity and enhances PD-1 checkpoint inhibition, our findings provide a mechanistic rationale for combining ECM-targeting strategies with immunotherapy. These findings not only deepen our understanding of the complex interplay between the HA-CD44 axis and the immune microenvironment but also provide a strong preclinical basis for targeting HA or CD44 as a strategy to overcome immunosuppression and enhance the efficacy of immunotherapy in this challenging disease.

Author affiliations
[1]Department of Gastrointestinal Surgery, Zhongshan Hospital, Fudan University, Shanghai, China
[2]Gastric Cancer Center, Zhongshan Hospital, Fudan University, Shanghai, China
[3]Department of General Surgery, Zhongshan Hospital (Xiamen), Fudan University, Xiamen, China
[4]Laboratory of Physiological Pathology, Nippon Veterinary and Life Science University, Musashino, Tokyo, Japan
[5]Department of Diagnostic Pathology, Fujita Health University School of Medicine Graduate School of Medicine, Toyoake, Aichi, Japan
[6]Department of Clinical Pharmaceutical Sciences, School of Pharmacy and 19 Pharmaceutical Sciences, Hoshi University, Tokyo, Japan
[7]Shanghai Clinical Research and Trial Center, ShanghaiTech University, Shanghai, China
[8]Department of Gastroenterology, Shanghai Ninth People's Hospital, School of Medicine, Shanghai Jiao Tong University, Shanghai, China
[9]Shanghai Key Laboratory of Gut Microecology and Associated Major Diseases Research, Shanghai, China

[10]Department of Biochemistry and Molecular Biology, School of Basic Medical Sciences, Fudan University, Shanghai, China
[11]Xiamen Clinical Research Center for Cancer Therapy, Xiamen, Fujian, China

Acknowledgements The authors thank Dr. Yitao Yuan and Dr. Wen Huang for FFPE slides diagnosis assistance. This work was also funded by the Outstanding Resident Clinical Postdoctoral Program of Zhongshan Hospital Affiliated to Fudan University.

Contributors Conceptualization: CJ and JZ; Methodology: CJ, JZ, ZW, BL, and YR. Data curation: CJ, CT, DL, ZS; Software and formal analysis: LS, CT, and GM; Resources: MY, TT, SN, TC, JS, and HL; Investigation: JS and HL; Writing of the original draft: CJ, JZ, and ZW; Writing of the review and editing: YR, LH, XW, and YS. Supervision, funding acquisition, and project administration: JZ, HL, XW, and YS. XW and HL are the guarantors. All the authors have read and approved the final manuscript.

Funding This work was supported by grants awarded to JZ (82002527) and XW (82573106) from the National Natural Science Foundation of China; awarded to XW (3502Z20224015) from the Project of Science and Technology of Xiamen City; awarded to HL (2024J011445) from the Project of Natural Science Foundation of Fujian Province; awared to ZW (23PJ1401400) from the project of Shanghai Pu Jiang Program.

Competing interests None declared.

Patient consent for publication Not applicable.

Ethics approval All experimental procedures involving human specimens and animals were in accordance with the ethical code and recommendation issued by Ethics Committee of Human Experimentation and Chinese Animal Community and with the Helsinki Declaration of 1975, as revised in 2008. The protocol of this study has been approved by the institutional review board and ethics committee of Zhongshan Hospital, Fudan University (B2023-123). All procedures of in vivo assays were conducted in accordance with protocols approved by the Animal Ethics Committee of Qishangbiomed IACUC (No:IACUC-ZSYY-2022107).

Provenance and peer review Not commissioned; externally peer reviewed.

Data availability statement Data are available upon reasonable request. Due to ethical and privacy considerations, the data are not publicly available but can be obtained from the corresponding author upon reasonable request.

Supplemental material This content has been supplied by the author(s). It has not been vetted by BMJ Publishing Group Limited (BMJ) and may not have been peer-reviewed. Any opinions or recommendations discussed are solely those of the author(s) and are not endorsed by BMJ. BMJ disclaims all liability and responsibility arising from any reliance placed on the content. Where the content includes any translated material, BMJ does not warrant the accuracy and reliability of the translations (including but not limited to local regulations, clinical guidelines, terminology, drug names and drug dosages), and is not responsible for any error and/or omissions arising from translation and adaptation or otherwise.

Open access This is an open access article distributed in accordance with the Creative Commons Attribution Non Commercial (CC BY-NC 4.0) license, which permits others to distribute, remix, adapt, build upon this work non-commercially, and license their derivative works on different terms, provided the original work is properly cited, appropriate credit is given, any changes made indicated, and the use is non-commercial. See https://creativecommons.org/licenses/by-nc/4.0/.

ORCID iDs
Chengbo Ji https://orcid.org/0000-0002-4394-8104
Dan Liu https://orcid.org/0009-0001-3009-3821
Xuefei Wang https://orcid.org/0000-0002-2645-0953

REFERENCES

1 Sung H, Ferlay J, Siegel RL, *et al*. Global Cancer Statistics 2020: GLOBOCAN Estimates of Incidence and Mortality Worldwide for 36 Cancers in 185 Countries. *CA Cancer J Clin* 2021;71:209–49.
2 Sasako M, Sano T, Yamamoto S, *et al*. D2 lymphadenectomy alone or with para-aortic nodal dissection for gastric cancer. *N Engl J Med* 2008;359:453–62.
3 Yoo CH, Noh SH, Shin DW, *et al*. Recurrence following curative resection for gastric carcinoma. *Br J Surg* 2000;87:236–42.
4 Ishizone S, Maruta F, Saito H, *et al*. Efficacy of S-1 for patients with peritoneal metastasis of gastric cancer. *Chemotherapy* 2006;52:301–7.
5 Thomassen I, van Gestel YR, van Ramshorst B, *et al*. Peritoneal carcinomatosis of gastric origin: a population-based study on incidence, survival and risk factors. *Int J Cancer* 2014;134:622–8.
6 Gwee YX, Chia DKA, So J, *et al*. Integration of Genomic Biology Into Therapeutic Strategies of Gastric Cancer Peritoneal Metastasis. *J Clin Oncol* 2022;40:2830.
7 Wang Y, Zhang X, Zhang Y, *et al*. Sprayed hyaluronic acid based multidrug composite hydrogel for postoperative colorectal cancer ultra-efficient long-lasting multi-stage immuno-chemo synergistic therapy. *Mater Horiz* 2025;12:4317–35.
8 Fang Z, Bunston C, Xu Y, *et al*. Implication of Capillary Morphogenesis Gene 2 (CMG2) in the Disease Progression and Peritoneal Metastasis of Pancreatic Cancer. *Cancers (Basel)* 2024;16:2893.
9 Soliman F, Ye L, Jiang W, *et al*. Targeting Hyaluronic Acid and Peritoneal Dissemination in Colorectal Cancer. *Clin Colorectal Cancer* 2022;21:e126–34.
10 Shariati M, Lollo G, Matha K, *et al*. Synergy between Intraperitoneal Aerosolization (PIPAC) and Cancer Nanomedicine: Cisplatin-Loaded Polyarginine-Hyaluronic Acid Nanocarriers Efficiently Eradicate Peritoneal Metastasis of Advanced Human Ovarian Cancer. *ACS Appl Mater Interfaces* 2020;12:29024–36.
11 Emoto S, Yamaguchi H, Kamei T, *et al*. Intraperitoneal administration of cisplatin via an in situ cross-linkable hyaluronic acid-based hydrogel for peritoneal dissemination of gastric cancer. *Surg Today* 2014;44:919–26.
12 Kitayama J, Ishigami H, Yamaguchi H, *et al*. Optimal drug delivery for intraperitoneal paclitaxel (PTX) in murine model. *Pleura Peritoneum* 2017;2:95–102.
13 Luo J, Wu Z, Lu Y, *et al*. Intraperitoneal administration of biocompatible hyaluronic acid hydrogel containing multi-chemotherapeutic agents for treatment of colorectal peritoneal carcinomatosis. *Int J Biol Macromol* 2020;152:718–26.
14 Valastyan S, Weinberg RA. Tumor metastasis: molecular insights and evolving paradigms. *Cell* 2011;147:275–92.
15 Ceelen WP, Bracke ME. Peritoneal minimal residual disease in colorectal cancer: mechanisms, prevention, and treatment. *Lancet Oncol* 2009;10:72–9.
16 Massagué J, Obenauf AC. Metastatic colonization by circulating tumour cells. *Nature New Biol* 2016;529:298–306.
17 Eyles J, Puaux A-L, Wang X, *et al*. Tumor cells disseminate early, but immunosurveillance limits metastatic outgrowth, in a mouse model of melanoma. *J Clin Invest* 2010;120:2030–9.
18 Paolino M, Choidas A, Wallner S, *et al*. The E3 ligase Cbl-b and TAM receptors regulate cancer metastasis via natural killer cells. *Nature New Biol* 2014;507:508–12.
19 Kitamura T, Qian BZ, Pollard JW. Immune cell promotion of metastasis. *Nat Rev Immunol* 2015;15:73–86.
20 Kamada T, Togashi Y, Tay C, *et al*. PD-1^{+} regulatory T cells amplified by PD-1 blockade promote hyperprogression of cancer. *Proc Natl Acad Sci U S A* 2019;116:9999–10008.
21 Togashi Y, Shitara K, Nishikawa H. Regulatory T cells in cancer immunosuppression - implications for anticancer therapy. *Nat Rev Clin Oncol* 2019;16:356–71.
22 Liu S, Liu Z, Shang A, *et al*. CD44 is a potential immunotherapeutic target and affects macrophage infiltration leading to poor prognosis. *Sci Rep* 2023;13:9657.
23 Ponta H, Sherman L, Herrlich PA. CD44: from adhesion molecules to signalling regulators. *Nat Rev Mol Cell Biol* 2003;4:33–45.
24 Ajani JA, Xu Y, Huo L, *et al*. YAP1 mediates gastric adenocarcinoma peritoneal metastases that are attenuated by YAP1 inhibition. *Gut* 2021;70:55–66.
25 Kotecha N, Krutzik PO, Irish JM. Web-Based Analysis and Publication of Flow Cytometry Experiments. *CP Cytometry* 2010;53.
26 Li H, Zhao J, Sun J, *et al*. Demethylation of the *SFRP4* Promoter Drives Gastric Cancer Progression via the Wnt Pathway. *Mol Cancer Res* 2021;19:1454–64.
27 Yaguchi T, Kobayashi A, Inozume T, *et al*. Human PBMC-transferred murine MHC class I/II-deficient NOG mice enable long-term evaluation of human immune responses. *Cell Mol Immunol* 2018;15:953–62.
28 Fujimori D, Kinoshita J, Yamaguchi T, *et al*. Established fibrous peritoneal metastasis in an immunocompetent mouse model similar to clinical immune microenvironment of gastric cancer. *BMC Cancer* 2020;20.
29 Yamamoto M, Nomura S, Hosoi A, *et al*. Established gastric cancer cell lines transplantable into C57BL/6 mice show fibroblast growth factor receptor 4 promotion of tumor growth. *Cancer Sci* 2018;109:1480–92.

30 Iwanicki MP, Davidowitz RA, Ng MR, *et al*. Ovarian cancer spheroids use myosin-generated force to clear the mesothelium. *Cancer Discov* 2011;1:144–57.
31 McGinnis CS, Murrow LM, Gartner ZJ. DoubletFinder: Doublet Detection in Single-Cell RNA Sequencing Data Using Artificial Nearest Neighbors. *Cell Syst* 2019;8:329–37.
32 Stuart T, Butler A, Hoffman P, *et al*. Comprehensive Integration of Single-Cell Data. *Cell* 2019;177:1888–902.
33 Macosko EZ, Basu A, Satija R, *et al*. Highly Parallel Genome-wide Expression Profiling of Individual Cells Using Nanoliter Droplets. *Cell* 2015;161:1202–14.
34 Aran D, Looney AP, Liu L, *et al*. Reference-based analysis of lung single-cell sequencing reveals a transitional profibrotic macrophage. *Nat Immunol* 2019;20:163–72.
35 Zhang X, Lan Y, Xu J, *et al*. CellMarker: a manually curated resource of cell markers in human and mouse. *Nucleic Acids Res* 2019;47:D721–8.
36 Alquicira-Hernandez J, Powell JE. Nebulosa recovers single-cell gene expression signals by kernel density estimation. *Bioinformatics* 2021;37:2485–7.
37 Gagneja S, Capalash N, Sharma P. Hyaluronic acid as a tumor progression agent and a potential chemotherapeutic biomolecule against cancer: A review on its dual role. *Int J Biol Macromol* 2024;275:133744.
38 Venet F, Chung C-S, Kherouf H, *et al*. Increased circulating regulatory T cells (CD4(+)CD25 (+)CD127 (-)) contribute to lymphocyte anergy in septic shock patients. *Intensive Care Med* 2009;35:678–86.
39 Wu C, Thalhamer T, Franca RF, *et al*. Galectin-9-CD44 interaction enhances stability and function of adaptive regulatory T cells. *Immunity* 2014;41:270–82.
40 The Cancer Genome Atlas Research Network. Comprehensive molecular characterization of gastric adenocarcinoma. *Nature New Biol* 2014;513:202–9.
41 Cristescu R, Lee J, Nebozhyn M, *et al*. Molecular analysis of gastric cancer identifies subtypes associated with distinct clinical outcomes. *Nat Med* 2015;21:449–56.
42 Wang R, Song S, Harada K, *et al*. Multiplex profiling of peritoneal metastases from gastric adenocarcinoma identified novel targets and molecular subtypes that predict treatment response. *Gut* 2020;69:18–31.
43 Yonemura Y, Canbay E, Li Y, *et al*. A comprehensive treatment for peritoneal metastases from gastric cancer with curative intent. *Eur J Surg Oncol* 2016;42:1123–31.
44 Joshi SS, Badgwell BD. Current treatment and recent progress in gastric cancer. *CA Cancer J Clin* 2021;71:264–79.
45 Zhao D, Yue P, Wang T, *et al*. Personalized analysis of minimal residual cancer cells in peritoneal lavage fluid predicts peritoneal dissemination of gastric cancer. *J Hematol Oncol* 2021;14:164.
46 Li J, Xu H, Zhang L, *et al*. Malignant ascites-derived organoid (MADO) cultures for gastric cancer in vitro modelling and drug screening. *J Cancer Res Clin Oncol* 2019;145:2637–47.
47 Nakano M, Ito M, Tanaka R, *et al*. Epithelial-mesenchymal transition is activated in CD44-positive malignant ascites tumor cells of gastrointestinal cancer. *Cancer Sci* 2018;109:3461–70.
48 Ray MD, Dhall K. Hyperthermic Intraperitoneal Chemotherapy (HIPEC) in the management of peritoneal surface malignancies - An evidence-based review. *Curr Probl Cancer* 2021;45:100737.
49 Yan TD, Black D, Sugarbaker PH, *et al*. A Systematic Review and Meta-analysis of the Randomized Controlled Trials on Adjuvant Intraperitoneal Chemotherapy for Resectable Gastric Cancer. *Ann Surg Oncol* 2007;14:2702–13.
50 Wang R, Dang M, Harada K, *et al*. Single-cell dissection of intratumoral heterogeneity and lineage diversity in metastatic gastric adenocarcinoma. *Nat Med* 2021;27:141–51.
51 Heldin P, Basu K, Olofsson B, *et al*. Deregulation of hyaluronan synthesis, degradation and binding promotes breast cancer. *J Biochem* 2013;154:395–408.
52 Chen C, Zhao S, Karnad A, *et al*. The biology and role of CD44 in cancer progression: therapeutic implications. *J Hematol Oncol* 2018;11:64.
53 Bao B, Tian M, Wang X, *et al*. SNORA37/CMTR1/ELAVL1 feedback loop drives gastric cancer progression via facilitating CD44 alternative splicing. *J Exp Clin Cancer Res* 2025;44:15.
54 Cao L, Weng K, Li L, *et al*. BATF2 inhibits the stem cell-like properties and chemoresistance of gastric cancer cells through PTEN/AKT/β-catenin pathway. *Theranostics* 2024;14:7007–22.
55 Thines L, Roushar FJ, Hedman AC, *et al*. The IQGAP scaffolds: Critical nodes bridging receptor activation to cellular signaling. *J Cell Biol* 2023;222.
56 Huang Y-T, Hsu Y-T, Wu P-Y, *et al*. Tight junction protein cingulin variant is associated with cancer susceptibility by overexpressed IQGAP1 and Rac1-dependent epithelial-mesenchymal transition. *J Exp Clin Cancer Res* 2024;43:65.
57 Wei T, Lambert PF. Role of IQGAP1 in Carcinogenesis. *Cancers (Basel)* 2021;13:3940.
58 Gorman JA, Babich A, Dick CJ, *et al*. The cytoskeletal adaptor protein IQGAP1 regulates TCR-mediated signaling and filamentous actin dynamics. *J Immunol* 2012;188:6135–44.
59 Peng JX, Liang SY, Li L. sFRP1 exerts effects on gastric cancer cells through GSK3β/Rac1-mediated restraint of TGFβ/Smad3 signaling. *Oncol Rep* 2019;41:224–34.